

REDSHIFT DISTRIBUTION OF EXTRAGALACTIC 24 μ m SOURCES^{1,2}

VANDANA DESAI^{3,4}, B. T. SOIFER^{3,4}, ARJUN DEY⁵, BUELL T. JANNUZI⁵, EMERIC LE FLOC'H^{6,7,8}, CHAO BIAN³,
KATE BRAND^{5,9}, MICHAEL J. I. BROWN¹⁰, LEE ARMUS⁴, DAN W. WEEDMAN¹¹, RICHARD COOL⁷, DANIEL STERN¹²,
MARK BRODWIN⁵

Accepted for publication in ApJ

ABSTRACT

We present the redshift distribution of a complete, unbiased sample of 24 μ m sources down to $f_{\nu}(24\mu\text{m}) = 300 \mu\text{Jy}$ (5σ). The sample consists of 591 sources detected in the Boötes field of the NOAO Deep Wide-Field Survey. We have obtained optical spectroscopic redshifts for 421 sources (71%). These have a redshift distribution peaking at $z \sim 0.3$, with a possible additional peak at $z \sim 0.9$, and objects detected out to $z = 4.5$. The spectra of the remaining 170 (29%) exhibit no strong emission lines from which to determine a redshift. We develop an algorithm to estimate the redshift distribution of these sources, based on the assumption that they have emission lines but that these lines are not observable due to the limited wavelength coverage of our spectroscopic observations. The redshift distribution derived from all 591 sources exhibits an additional peak of extremely luminous ($L_{8-1000\mu\text{m}} > 3 \times 10^{12} L_{\odot}$) objects at $z \sim 2$, consisting primarily of sources without observable emission lines. We use optical line diagnostics and IRAC colors to estimate that 55% of the sources within this peak are AGN-dominated. We compare our results to published models of the evolution of infrared luminous galaxies. The models which best reproduce our observations predict a large population of star-formation dominated ULIRGs at $z > 1.5$ rather than the AGN-dominated sources we observe.

Subject headings: galaxies: distances and redshifts — galaxies: evolution — galaxies: formation — infrared: galaxies

1. INTRODUCTION

An important goal in extragalactic astronomy is to understand when, where, and how the stellar content of the universe formed. Based on rest-frame ultraviolet and optical measures, the star formation rate per comoving volume is approximately constant from $z \approx 6$ to $z \approx 2$ and then smoothly decreases by a factor of ten until the present epoch (Gallego et al. 1995; Lilly et al. 1996; Madau et al. 1996; Connolly et al. 1997; Treyer et al. 1998; Flores et al. 1999; Steidel et al. 1999; Wilson et al. 2002; Giavalisco et al. 2004). There is also increasing evidence that galaxies with large stellar masses formed most of their stars earlier than lower-mass galaxies

(Tinsley 1968; Cowie et al. 1996; Heavens et al. 2004; Juneau et al. 2005).

Observations of the far-infrared background radiation with the *Cosmic Background Explorer* (COBE; Puget et al. 1996; Fixsen et al. 1998; Hauser et al. 1998; Dwek et al. 1998; Lagache et al. 1999; Lagache & Puget 2000; Finkbeiner et al. 2000) show that the infrared energy density is comparable to the combined UV, visible, and near-infrared energy density, indicating that half of the light originally emitted in the UV and optical has been intercepted by dust, reprocessed, and re-emitted in the infrared (Gispert et al. 2000). What kinds of galaxies contribute to the infrared peak in the extragalactic background light? The earliest mid-infrared observations of extragalactic sources revealed a class of galaxies which emit the bulk of their luminosity in the infrared (Low & Kleinmann 1968; Kleinmann & Low 1970a,b; Rieke & Low 1972). Early observations with the *Infrared Astronomical Satellite* (IRAS) showed that luminous infrared galaxies (LIRGs; $10^{11} < L_{8-1000\mu\text{m}}(L_{\odot}) < 10^{12}$) and ultraluminous infrared galaxies (ULIRGs; $L_{8-1000\mu\text{m}} > 10^{12} L_{\odot}$) do not contribute substantially to the total infrared emission in the local ($z < 0.05$) universe (Soifer & Neugebauer 1991).

However, there is strong evidence that infrared-bright populations become more significant at higher redshift. This evidence includes number counts obtained with *IRAS* (Hacking et al. 1987) and the *Infrared Space Observatory* (*ISO*; Oliver et al. 1997; Altieri et al. 1999; Aussel et al. 1999; Elbaz et al. 1999; Gruppioni et al. 2002; Metcalfe et al. 2003). Spectroscopic follow-up of these sources has directly confirmed the increasing significance of the infrared-bright population out to $z \sim 0.3$

¹ Based on observations made with the *Spitzer Space Telescope*, operated by the Jet Propulsion Laboratory under NASA contract 1407.

² Some of the data presented herein were obtained at the W. M. Keck Observatory, which is operated as a scientific partnership among the California Institute of Technology, the University of California, and the National Aeronautics and Space Administration. The Observatory was made possible by the generous financial support of the W. M. Keck Foundation.

³ Division of Physics, Mathematics and Astronomy, California Institute of Technology, Pasadena CA 91125

⁴ Spitzer Science Center, California Institute of Technology, Pasadena CA 91125

⁵ National Optical Astronomy Observatory, Tucson AZ 85726-6732

⁶ Spitzer Fellow

⁷ Steward Observatory, University of Arizona, Tucson AZ 85721

⁸ Institute for Astronomy, University of Hawaii, Honolulu HI 96822

⁹ Space Telescope Science Institute, Baltimore MD 21218

¹⁰ School of Physics, Monash University, Clayton, Victoria 3800, Australia

¹¹ Astronomy Department, Cornell University, Ithaca NY 14853

¹² Jet Propulsion Laboratory, California Institute of Technology, Pasadena CA 91109

(Kim et al. 1998; Serjeant et al. 2001), a redshift set by the sensitivity limits of the existing mid-infrared surveys. Progress in constraining the population of infrared-luminous galaxies at higher redshift has been made via surveys at submillimeter (e.g. Smail et al. 1997; Chapman et al. 2001; Blain et al. 2002) and radio (Cowie et al. 2004) wavelengths. These data provide further evidence of strong evolution in the infrared-luminous population, but the number of sources probed are small, and may suffer from selection biases. For instance, spectroscopy of submillimeter sources has relied on accurate positions obtained from radio counterparts, biasing spectroscopic samples to sources that are bright in both the submillimeter and the radio (Chapman et al. 2005). The sensitive Multiband Imaging Photometer for the *Spitzer Space Telescope* (MIPS; Rieke et al. 2004; Werner et al. 2004) has allowed the detection of many faint infrared sources. Number counts at $24\ \mu\text{m}$ determined by *Spitzer* observations confirm the strong evolution previously observed in the infrared luminous population (Chary et al. 2004; Dole et al. 2004; Marleau et al. 2004; Papovich et al. 2004).

Although number counts provide valuable information on the evolution of the infrared population, they do not allow a robust distinction between luminosity and density evolution. For this, redshifts are needed. The redshift distribution is shaped by the evolution of galaxy SEDs and luminosity functions, which in turn depend on the physics of galaxy evolution: star formation, AGN activity, dust obscuration, mergers, and feedback (Lagache et al. 2005). The redshift distribution is therefore a useful constraint on the importance of these processes.

Several attempts have been made to estimate the redshift distribution of $24\ \mu\text{m}$ sources using photometric redshifts. For sources with $f_\nu(24\mu\text{m}) > 83\ \mu\text{Jy}$, these studies consistently reveal a primary peak in the redshift distribution at $z < 1$, with small differences in the precise location of this peak attributable to cosmic variance (Pérez-González et al. 2005; Le Floc'h et al. 2005; Caputi et al. 2006; Papovich et al. 2007). Such a peak can be attributed to strong luminosity and/or density evolution in the infrared population out to $z \sim 1$ (Chary & Elbaz 2001; Lagache et al. 2004; Gruppioni et al. 2005; Pérez-González et al. 2005). However, contradictory results are found for the existence of a predicted secondary peak at $z \sim 2$ (Pérez-González et al. 2005; Caputi et al. 2006). Such a secondary peak may be expected from a significant high-redshift population of either highly absorbed AGN-dominated sources or PAH-rich starburst-dominated sources. These would have a local peak in their SEDs at $\approx 8\ \mu\text{m}$, due either to continuum adjacent to deep absorption features or to line emission, respectively. This $8\ \mu\text{m}$ peak would enhance the detectability of these sources at $z \approx 2$ in $24\ \mu\text{m}$ surveys. Uncertainties in the photometric redshifts may be responsible for the contradictory observational results regarding the existence of this peak, since previous studies have few ($\lesssim 25$) spectroscopic redshifts above $z = 1.5$. Photometric estimates of the redshift distribution for more shallow surveys ($f_\nu(24\mu\text{m}) \gtrsim 200\ \mu\text{Jy}$) also produce mixed results for the $z \sim 2$ peak (Rowan-Robinson et al. 2005; Babbage et al. 2006). Recent spectroscopic surveys of

$24\ \mu\text{m}$ sources are complete only to about the same redshift ($z \sim 1$) reliably probed by photometric redshifts (Papovich et al. 2006; Marleau et al. 2007).

In this work, we present new measurements of the redshift distribution of $24\ \mu\text{m}$ sources down to $300\ \mu\text{Jy}$. Our sample is selected from 23 noncontiguous areas spread across $8.74\ \text{deg}^2$ of the $24\ \mu\text{m}$ map of the Boötes field of the NOAO Deep Wide-Field Survey (NDWFS; Jannuzi & Dey 1999). Our results are therefore minimally affected by variations in the density of the $24\ \mu\text{m}$ source population due to structures on the scale of $\sim 0.5\ \text{deg}^2$. Although our sample is modest (591 sources; comparable in size to the smaller studies mentioned above), a larger fraction (71%) have spectroscopic redshifts. The remaining 29% exhibit no spectral features from which to determine a redshift. Given the limitations of photometric redshifts for $24\ \mu\text{m}$ sources at $z > 1$, we have developed an algorithm for estimating the redshift distribution of this population from their continuum spectra. Briefly, this described (algorithm in detail in §5.2) is based on the assumptions that bright $24\ \mu\text{m}$ sources are undergoing strong star formation and/or AGN activity, and the emission lines resulting from this activity are able to penetrate the surrounding dust. These assumptions hold true for $\approx 70\%$ of the $24\ \mu\text{m}$ sources in our sample, and also hold for very obscured local ultraluminous infrared sources (e.g. Sanders et al. 1988a; Kleinmann et al. 1988; Armus et al. 1989; Allen et al. 1991; Cutri et al. 1994; Veilleux et al. 1995, 1997; Duc et al. 1997). Under these assumptions, the lack of observed emission lines for certain sources is due to the limited wavelength coverage of our spectroscopic observations.

We describe our targeting strategy in §2, our targeting completeness in §3, and our spectroscopic observations in §4. Our results are presented in §5. In particular, we present the redshift distribution of emission-line galaxies (§5.1), the redshift distribution of galaxies that exhibit no emission lines (§5.2), and the redshift distribution for the entire sample (§5.3). In §6, we discuss the shape of the overall redshift distribution and compare our observations to existing models of the evolution of infrared galaxies. Finally, we summarize our conclusions in §7. All calculations are carried out assuming a cosmology with $H_0 = 70\ \text{km s}^{-1}\ \text{Mpc}^{-1}$, $\Omega_0 = 0.3$, and $\Omega_\Lambda = 0.7$.

2. TARGETING STRATEGY

We have conducted an optical spectroscopic survey of ~ 600 $24\ \mu\text{m}$ sources in order to determine their redshift distribution. The spectroscopic targets were drawn from a catalog of $\sim 22,000$ sources detected in a MIPS survey of $8.74\ \text{deg}^2$ of the Boötes field of the NDWFS. The 5σ point-source depth of the imaging is $300\ \mu\text{Jy}$, and this sets the flux limit of both the detection catalog and our spectroscopic survey.

The spectroscopy was carried out using the Deep Imaging Multi-Object Spectrograph (DEIMOS; Faber et al. 2003) and the Low Resolution Imaging Spectrometer (LRIS; Oke et al. 1995), both on the W. M. Keck 10-meter telescopes. In total, we observed 11 DEIMOS and 12 LRIS masks. Mask positions were chosen to maximize the number of high-priority targets, which are defined to be sources with $f_\nu(24\mu\text{m}) > 750\ \mu\text{Jy}$ and faint optical magnitudes ($R > 24\ \text{mag}$ or $f_\nu(R) < 0.74\ \mu\text{Jy}$). Figure 1 shows the positions of the masks on the sky. The remain-

ing targets on each mask were selected from the sources with $f_\nu(24\mu\text{m}) \geq 300 \mu\text{Jy}$, without regard to $R - [24]$ color. To $f_\nu(24\mu\text{m}) \geq 300 \mu\text{Jy}$, 24 μm sources have a surface density of about 2400 deg^{-2} . There are ≈ 50 per 0.02 deg^2 DEIMOS mask and ≈ 25 per 0.01 deg^2 LRIS mask, resulting in a total of 818 over the 0.33 deg^2 combined mask area. We targeted 544, or 67%. (Our final sample includes 47 supplementary sources described in Section 3.) The untargeted sources were excluded mainly due to slit collisions. In the case of slit collisions, we preferentially targeted faint (but not invisible) optical sources. Although their combined area is modest, our spectroscopic masks span 8.74 deg^2 of the Boötes field. This makes our survey less subject to the effects of cosmic variance due to structures on the scale of approximately half a square degree.

In designing the spectroscopic masks, we attempted to position the slits on the optical (R -band) counterparts of the 24 μm targets. For reference, the NDWFS R -band imaging has a 3σ point-source depth of ~ 26 Vega magnitudes.¹³ The position of the optical counterpart was determined in the following way. For each 24 μm source, the SExtractor R -band catalog was searched for nearby sources. For extended sources, we match detections in different bands when their centroids are within an ellipse defined by the second-order moments of the optical light distribution (as defined by SExtractor). For both compact and extended sources we match detections in different bands when their centroids are within $1''$ of each other. When matching bright sources, where centroids in different bands can be offset or optical sources are well resolved, matching MIPS sources to SExtractor catalogs has some advantages over simple R -band aperture photometry at the position of the MIPS source. When there are multiple R -band detections which meet our matching criteria, our code opts for the closest centroid. The plots in this paper show magnitudes computed within a $4''$ diameter aperture. In some cases, we find no R -band counterpart. After visual inspection of these cases, we perform R -band aperture photometry at the MIPS position. The optical positions determined by the above method were used as a starting point for designing the slit masks. The final slit positions were adjusted based on visual inspection of the R -band and 24 μm images, as well as additional imaging (Eisenhardt et al. 2004) acquired with *Spitzer's* Infrared Array Camera (IRAC; Fazio et al. 2004). The IRAC images were useful in identifying ambiguous optical counterparts, since the MIPS targets are all detected by IRAC, which has a much smaller PSF than MIPS. In addition, sometimes faint optical counterparts can be identified by eye even if they did not appear in the R -band SExtractor catalog.

3. TARGETING COMPLETENESS

In the following, the term “Keck spectroscopic targets” refers to both the high-priority targets and the flux-limited targets described above. The inclusion of high-priority sources as well as the preference for faint R -band sources in cases of slit collisions mean that our sample of Keck spectroscopic targets is not completely unbiased. Figure 2 shows the differential and cumulative distribu-

tions of $R - [24]$ colors for all of the $f_\nu(24\mu\text{m}) \geq 300 \mu\text{Jy}$ sources within the Keck survey region and for the subset of these that were targeted for spectroscopy. A two-sided Kolmogorov-Smirnov (KS) test shows that the 24 μm flux density distributions of these two sets of galaxies are indistinguishable. In contrast, their R -band magnitude and $R - [24]$ color distributions are different at a statistically significant level, in the sense that our target list includes an excess of optically faint, red sources.

To correct this bias, we supplement our Keck spectroscopic targets with 47 optically bright ($R < 23 \text{ mag}$) sources within the Keck survey region that were not targeted with LRIS or DEIMOS, but which have redshifts from the AGN and Galaxy Evolution Survey (AGES; Kochanek et al. in preparation). AGES is a spectroscopic survey of galaxies ($I < 20 \text{ mag}$) and AGN ($I < 21.5 \text{ mag}$) in the NDWFS Boötes field carried out with the Hectospec instrument (Fabricant et al. 2005) on the MMT. We selected the supplementary AGES sample randomly under the requirement that each 0.1 R -band magnitude bin at $R < 23 \text{ mag}$ have the same sampling fraction as the average Keck sampling fraction at $R > 23 \text{ mag}$ (74%). The differential and cumulative distributions of $R - [24]$ colors for the combined Keck and supplementary AGES targets are shown in Figure 2. Two-sided Kolmogorov-Smirnov tests confirm that the Keck+AGES sample is fairly drawn from the population of sources with $f_\nu(24\mu\text{m}) > 300 \mu\text{Jy}$ that lie within the Keck spectroscopic survey area, in terms of $f_\nu(24\mu\text{m})$, R -band magnitude, and $R - [24]$ color. Thus we conclude that the Keck+AGES targets are an unbiased sample of sources selected at 24 μm .

4. SPECTROSCOPIC OBSERVATIONS

The DEIMOS and LRIS optical spectroscopic followup of 24 μm sources was carried out in May 2004 and May 2005. The DEIMOS observations for each mask are composed of 3-4 frames lasting 20 or 30 minutes each, resulting in total exposure times of 90-120 minutes per mask. The 600 line mm^{-1} (7500 Å blaze) grating was used with the GG400 blocking filter, resulting in a mean spectral dispersion of $0.65 \text{ Å pixel}^{-1}$. The central wavelength was set to 7500 Å. We typically used $1.0''$ wide by $10''$ long slitlets, corresponding to a FWHM spectral resolution of 4.6 Å. Although the wavelength coverage varies with slit position, a typical DEIMOS spectrum ranges from 5200-10200 Å. We used the DEEP2 data reduction pipeline¹⁴ to perform cosmic ray removal, flat-fielding, co-addition, sky-subtraction, and wavelength calibration. The one-dimensional spectra were extracted using standard IRAF¹⁵ routines (Tody 1993).

The LRIS observations are also composed of 3-4 frames lasting 20 or 30 minutes each, yielding total exposure times of 60-120 minutes per mask. One mask was observed for a total of only 20 minutes. The telescope was offset by a few arcseconds between frames. The slitlets were $1''$ wide by $11''$ long. LRIS was configured with the 5600 Å dichroic. On the blue side, we used the 400 line mm^{-1} grism with a central wavelength of 3400 Å,

¹⁴ <http://alamoana.ck.hawaii.edu/inst/deimos/pipeline.html>

¹³ See <http://www.noao.edu/noao/noaodeep/> for more information regarding the depth and coverage of the NDWFS.

¹⁵ IRAF is distributed by the National Optical Astronomy Observatory, which is operated by the Association of Universities for Research in Astronomy, Inc., under cooperative agreement with the National Science Foundation.

resulting in a spectral dispersion of $1.09 \text{ \AA pixel}^{-1}$ and a FWHM spectral resolution of 6.9 \AA . On the red side, we used the 400 line mm^{-1} grating with a central wavelength of 8500 \AA , resulting in a spectral dispersion of $1.86 \text{ \AA pixel}^{-1}$ and a FWHM spectral resolution of 7.5 \AA . Our LRIS spectra typically have a wavelength coverage of $2200\text{--}8200 \text{ \AA}$. We used an IRAF package called BOGUS¹⁶ to reduce the two-dimensional spectra. The one-dimensional spectra were extracted using standard IRAF routines.

Relative spectrophotometric calibration for both the DEIMOS and LRIS observations was performed using observations of Wolf 1346 (Massey et al. 1988; Massey & Gronwall 1990; Oke 1990).

5. RESULTS

Our primary observational result is the redshift distribution of $24 \text{ }\mu\text{m}$ sources down to $300 \text{ }\mu\text{Jy}$. In the following three subsections, we present the redshift distributions of the sources with detected emission lines, of the sources without detected emission lines, and of the entire sample.

5.1. Redshift Distribution of Galaxies with Detected Emission Lines

Each of the one- and two-dimensional DEIMOS and LRIS spectra were visually inspected for spectral lines from which redshifts could be measured. Some example spectra are shown in Figure 3, and many more will be provided in a forthcoming paper (Soifer et al. in preparation). Out of the 544 sources that were targeted, 368 spectra (69%) yielded redshifts. Two or more spectral lines were typically available to determine a redshift. In 44 cases (12%), only one spectral line was observed. Eight of these had absorption features in the Keck spectrum or additional features from AGES spectra that helped to determine the redshift. In the remaining spectra, the single observed emission line was identified based on its shape and width as $\text{Ly}\alpha$ in eight cases, $\text{MgII}\lambda 2798$ in three cases, and $[\text{OII}]\lambda 3727$ in 25 cases. These single-line sources are included in our sample with spectroscopic redshifts.

Of the 176 galaxies that we targeted with either DEIMOS or LRIS but for which we were unable to determine a redshift, six of these were bright enough in the optical ($R = 21.16, 16.58, 19.42, 22.15, 20.12, 18.30 \text{ mag}$) to have redshifts from the AGES Survey. The AGES redshifts are $z = 1.799, 0.076, 2.230, 1.509, 0.545$, and 1.069 . The DEIMOS spectrum of the $z = 0.076$ source did not yield a redshift because it was saturated. The LRIS spectrum of the $z = 0.545$ source showed absorption lines, but identifiable emission lines were lost in the gap between the red and blue sides. The differing wavelength coverage of the Keck spectrographs compared to Hectospec explains the remaining sources. The AGES data bring the number of Keck targets with redshifts up to 374. Hereafter, we refer to the redshifts of all Keck targets with either Keck or AGES spectroscopic redshifts as the Keck sample. In contrast, the Keck targets supplemented with sources with bright optical fluxes from AGES, as described in §3, will be referred to as the Keck+AGES sample.

Figure 4 shows the R -band magnitudes versus $24 \text{ }\mu\text{m}$ flux densities for the Keck+AGES targets, for the sources in the spectroscopic survey region that were not included in the Keck+AGES target list, for the Keck+AGES targets with spectroscopic redshifts, and for the Keck targets without spectroscopic redshifts. This figure illustrates that the $24 \text{ }\mu\text{m}$ flux density is only weakly correlated with the R -band magnitude, and that the Keck targets for which we were unable to determine spectroscopic redshifts are mostly faint in the optical ($R > 21 \text{ Vega mag}$), but span a range in $24 \text{ }\mu\text{m}$ flux densities.

Figure 5 shows the success rate in determining redshifts for Keck and Keck+AGES targets as functions of $24 \text{ }\mu\text{m}$ flux density, R -band magnitude, and $R - [24]$ color. This success rate is a strong function of R -band magnitude, and drops below 50% for $R > 23.5 \text{ mag}$. This dependence on R -band magnitude propagates into a dependence on the $R - [24]$ color. In contrast, the redshift success rate is a much weaker function of $24 \text{ }\mu\text{m}$ flux density.

Figure 6 shows the $24 \text{ }\mu\text{m}$ flux density, R -band magnitude, and $R - [24]$ color versus redshift for the sources with spectroscopic redshifts. The $24 \text{ }\mu\text{m}$ flux density is not tightly correlated with redshift. In contrast, both the R -band magnitudes and the $R - [24]$ colors of the majority of these same sources correlate strongly with redshift out to $z = 1$. At larger redshifts, the scatter increases substantially.

For each source with an emission line redshift, Figure 7 shows the νL_ν luminosity at the rest wavelength probed by the MIPS $24 \text{ }\mu\text{m}$ filter at the observed redshift. The luminosity-dependent SEDs developed for the Chary & Elbaz (2001) models are used to indicate the regions of this plot occupied by normal galaxies, LIRGs, ULIRGs, and HyperLIRGs. This figure shows that the $24 \text{ }\mu\text{m}$ sources in our sample span a large range in bolometric luminosities.

5.2. Redshift Distribution of Galaxies without Emission Lines

We were unable to determine emission line redshifts for 170 Keck targets (124 DEIMOS targets and 46 LRIS targets). Visual inspection of the optical, IRAC, and MIPS imaging suggests that the optical counterpart may have been incorrectly targeted in up to 20% of these sources. Generally, this uncertainty is due to the faintness of the optical counterpart combined with the large $24 \text{ }\mu\text{m}$ beam size. A quarter of the time, the uncertainty stems from a choice between multiple optical counterparts. Despite this uncertainty, we use the following algorithm to estimate the redshift distribution of these sources.

First, we assume that these sources lie at $z < 4.5$. This is the highest emission-line redshift found in our survey. This redshift cut-off is further justified by the fact that a $z > 4.5$ source with $f_\nu(24\mu\text{m}) \geq 300 \text{ }\mu\text{Jy}$ would have a luminosity of $L_{8-1000\mu\text{m}} > 3.5 \times 10^{13} L_\odot$ (assuming the templates of Chary & Elbaz (2001)). Galaxies with such extreme luminosities should be exceedingly rare.

Second, we assume that $24 \text{ }\mu\text{m}$ sources that are well-detected in the bluest NDWFS filter ($B_W < 25 \text{ mag}$) must lie at $z < 3$. This ensures that some part of the B_W filter (which covers the approximate wavelength range $3500\text{--}4750 \text{ \AA}$) is sampling rest-frame wavelengths longward of the Lyman break.

¹⁶ <https://zwolfkinder.jpl.nasa.gov/~stern/homepage/bogus.html>

Third, we assume that all bright MIPS sources should be undergoing strong star formation and/or AGN activity, and should therefore harbor the conditions required to produce strong emission lines, including Ly α , [OII] λ 3727, H β , and H α . Although red sources that are bright at 24 μm must be dusty, these emission lines are able to penetrate the dust for the majority of our targets. This is likely due to the fact that the dust obscuration is patchy, allowing optical/UV emission lines to be observed in very obscured sources. In fact, many very obscured local ultraluminous infrared galaxies, including Arp 220, display strong emission lines which dominate their optical spectra (Duc et al. 1997; Veilleux et al. 1997, 1995; Cutri et al. 1994; Allen et al. 1991; Armus et al. 1989; Kleinmann et al. 1988; Sanders et al. 1988b). We assume that this is the case for the targets without detected emission lines as well, and that the lack of observed emission lines is due to insufficient wavelength coverage rather than to intrinsically weak or completely obscured emission lines. Below we describe how we rule out those redshifts for which any one of Ly α , [OII] λ 3727, H β , or H α could have been detected.

We assume that a line could have been detected at a particular wavelength (corresponding to a specific redshift) if the limiting rest-frame equivalent width at that wavelength is smaller than a fiducial rest-frame equivalent width, which we take to be 10 \AA for each of the four emission lines we are considering. For each spectrum, we determined the limiting rest-frame equivalent width as a function of wavelength following Equation 4 in Hogg et al. (1998):

$$\text{EQW}_{\text{lim,rest}}(\lambda) = \frac{\eta\lambda_1}{r(\lambda)} \left(\frac{\Delta\lambda}{\lambda_1} \right)^{1/2} [1 + z(\lambda)]^{-1/2}. \quad (1)$$

Here, η is the minimum signal-to-noise ratio required for the line to be detected, and was taken to be three for both LRIS and DEIMOS spectra, and for all four emission lines. The variable $r(\lambda)$ is the signal-to-noise ratio of the extracted spectrum as a function of wavelength. It was computed by convolving the extracted spectrum with a Gaussian kernel characterized by a FWHM of 200 \AA , and dividing the result by the noise within a moving bin of 13 pixels in the (unconvolved) extracted spectrum. The spectral dispersion, λ_1 , is 0.65 \AA pixel^{-1} for DEIMOS, 1.09 \AA pixel^{-1} for the blue side of LRIS, and 1.86 \AA pixel^{-1} for the red side of LRIS. The parameter $\Delta\lambda$ is the rest-frame FWHM of the emission line in question, which we take to be 10 \AA for all four emission lines. Finally, z is the redshift which corresponds to the wavelength at which we are computing the rest-frame limiting EQW, and is given by $z = (\lambda/\lambda_{\text{rest}}) - 1$, where $\lambda_{\text{rest}} = 1216, 3727, 4861, 6563 \text{ \AA}$ for Ly α , [OII], H β , and H α , respectively.

After ruling out those redshifts at which these emission lines could have been detected for each individual source, we constructed a redshift probability distribution function for the ensemble by summing the number of sources that could lie at a given redshift, and normalizing the result to a total probability of unity. This is based on the assumption that each galaxy has a uniform probability of lying at any redshift that is not ruled out by the above three arguments (that all 24 μm sources lie at

$z < 4$, that all 24 μm sources that are well-detected in B_W must lie at $z < 3$, and that all 24 μm sources must have strong emission lines that have gone undetected due to limited spectral coverage). Figure 8 shows the result for all of the targets without redshifts, and for those observed with DEIMOS and LRIS separately. Based on the lack of the [OII] λ 3727 emission line in their spectra, most of the sources observed with DEIMOS are unlikely to lie at $z < 1.5$. In addition, few lie at $z > 3.5$, or else we would have observed Ly α . In contrast, the redshift distribution of the sources observed with LRIS is closer to uniform. The similarity of the top and bottom panels of Figure 8 reflects the fact that most of the targets without spectroscopic redshifts were observed with DEIMOS.

Figure 8 does not take into account the fact that the mean luminosity of galaxies in a flux-limited survey increases with redshift and the luminosity function decreases rapidly at the high-luminosity end. Qualitatively, this means that a galaxy does not have an equal probability of lying at every redshift not ruled out by the above algorithm. A given galaxy is more likely to be an L_* galaxy at moderate redshift than five times more luminous at a higher redshift. However, given the limited photometric information available to derive a luminosity at a common wavelength for each galaxy, we do not attempt to quantify this qualitative statement.

5.3. Redshift Distribution

The redshift distribution of the Keck+AGES targets is shown in Figure 9. The contributions of the following categories of sources are indicated separately: the Keck targets with emission-line redshifts; the supplementary AGES sample selected to correct the bias of the Keck spectroscopic targeting against bright optical sources; and Keck targets without spectroscopic redshifts, assuming that they all have emission lines that could not be observed due to the limited wavelength coverage of the Keck spectrographs and that they have an equal probability of lying at any redshift in the range $0 < z < 4.5$ that is not excluded by the lack of detected emission lines (see Section 5.2). Figure 9 shows that the galaxies with spectroscopic redshifts peak at $z \sim 0.3$. The majority of the targets without emission lines cannot lie at this redshift or [OII] λ 3727 would have been observed. Instead, most of these sources are constrained to lie at $2 < z < 3$, where [OII] λ 3727 lies longward of the observed spectrum and Ly α lies shortward of it. These sources appear in the redshift distribution as a weak second peak at $z \sim 2$.

6. DISCUSSION

6.1. Shape of the Redshift Distribution

The redshift distribution of 24 μm sources is expected to be shaped both by evolution in the infrared luminosity function and by major features in the mid-infrared spectra of luminous infrared galaxies. These in turn depend upon fundamental processes governing galaxy evolution, such as star formation, AGN activity, dust obscuration, galaxy mergers, and feedback from supernovae and AGN. Thus, the redshift distribution is an important constraint on models of these processes.

In the absence of any evolution, the number of sources observed in a given redshift bin depends only on the volume probed by that bin, the range of luminosities probed

by that bin, and the shape of the $z = 0$ luminosity function. The first two effects act in opposite directions: volume increases with redshift, leading to an increase in the observed number of galaxies with redshift. However, the flux limit means that a decreasing range of luminosities, and therefore a decreasing number of galaxies, is observed with increasing redshift. How does an evolving luminosity function affect the redshift distribution? A decrease in either the space density or the characteristic luminosity of infrared sources with redshift would cause fewer galaxies to be observed at high redshift. Conversely, an increase in the space density or characteristic luminosity would appear as a rise in the redshift distribution.

In addition to a strong dependence on the evolving luminosity function, the observed redshift distribution is also affected by prominent features in the mid-infrared spectra of infrared sources. A strong emission feature can increase the observed broadband MIPS $24\ \mu\text{m}$ flux density of a galaxy. Thus, objects with strong emission features can be pushed into a flux-limited sample, even if they would not be targeted based on their continua alone. Conversely, sources with strong absorption features can fall out of flux-limited samples. The strongest mid-infrared spectral features in LIRGs and ULIRGs are the silicate absorption feature at rest-frame $9.7\ \mu\text{m}$ and the Polycyclic Aromatic Hydrocarbon (PAH) emission features at rest-frame wavelengths $3.3, 6.2, 7.7, 8.6, 11.3, 12.7, 16.3$, and $17\ \mu\text{m}$. The redshift distribution of $24\ \mu\text{m}$ sources may display troughs and peaks at redshifts corresponding to the presence of these absorption and emission features in the observed $24\ \mu\text{m}$ bandpass, and therefore contains information about the types of galaxies at each redshift. In this subsection, we consider the most prominent features of the observed redshift distribution shown in Figure 9, compare to the results of previous observations, and discuss their possible origins.

Figure 9 shows a strong increase in the number of sources from $z = 0$ to $z \sim 0.3$. A rise is also seen at $z < 1$ by Pérez-González et al. (2005), Le Floch et al. (2005), and Caputi et al. (2006). However, the peak in these studies occurs at higher redshifts ($z \sim 0.8$), presumably because they have a deeper $24\ \mu\text{m}$ flux density limit ($83\ \mu\text{Jy}$ versus our $300\ \mu\text{Jy}$). As discussed above, a rise in the redshift distribution could be caused by a strong spectral feature entering the $24\ \mu\text{m}$ bandpass, by evolution in the luminosity function, or simply by the fact that larger volumes are probed at higher redshifts. There are no strong spectral features that could be causing the $z \sim 0.3$ peak. The detailed modeling that is required to distinguish between the remaining scenarios is beyond the scope of this paper. However, in §6.2 we compare our observations to existing phenomenological models of the evolving luminosity function.

There is potentially another peak in the redshift distribution at $z \sim 0.9$. However, it is very weak, and has not been seen in the previous measurements of the redshift distribution described in §1. Given the small areas of the previous surveys, this could very well be due to cosmic variance (see Somerville et al. (2004)). Additional possibilities include the fact that most previous efforts were either incomplete at these redshifts, or based on photometric redshifts, which would tend to smooth out features in the intrinsic redshift distribution. If real, this

peak could be the result of the $12.7\ \mu\text{m}$ PAH feature and the $12.8\ \mu\text{m}$ [NeII] emission line passing through the $24\ \mu\text{m}$ bandpass.

Between $z \sim 0.8$ and $z \sim 1.6$, the redshift distribution exhibits a steep decline, which has also been reported by Pérez-González et al. (2005) and Caputi et al. (2006). Such a decline could be the result of a flattening or a drop in either the density or the characteristic luminosity of infrared galaxies. A decline could also result if a significant fraction of sources with $f_\nu(24\ \mu\text{m}) \geq 300\ \mu\text{Jy}$ have deep silicate absorption features at rest-frame $9.7\ \mu\text{m}$. Some highly absorbed sources may fall below the sample's flux limit as the absorption feature enters the $24\ \mu\text{m}$ bandpass. This would result in a broad dip centered at $z \sim 1.5$, the redshift at which the center of the broad absorption feature coincides with the center of the wide bandpass.

Also visible in the redshift distribution is a possible peak at $z \sim 2$. However, Figure 9 clearly shows that this peak is composed mostly of sources for which we were unable to determine spectroscopic redshifts due to the lack of observed emission lines. We remind the reader that we constrained the redshift distribution of such sources by assuming that 1) these non-detections were due to the limited wavelength coverage of optical spectrographs; 2) $24\ \mu\text{m}$ sources that are well-detected in the bluest ND-WFS filter ($B_W < 25\ \text{mag}$) must lie at $z < 3$ so that some part of the B_W filter is sampling rest-frame wavelengths longward of the Lyman break; and 3) there are no $24\ \mu\text{m}$ sources at redshifts larger than $z = 4.5$ (see §5.2). The exact location of the $z \sim 2$ peak is uncertain because we have assumed that a given galaxy is equally likely to lie at any redshift not ruled out by the previous three assumptions.

In the future, it will be possible to provide stronger constraints on the redshift distribution of the mid-infrared sources which lack spectroscopic redshifts by incorporating priors associated with the mid-infrared luminosities, optical luminosities, and colors of the sources. However, adding priors to our estimate at the present time is complicated for many reasons. First, there is no well-measured luminosity function for $24\ \mu\text{m}$ sources at high redshift. The current best luminosity functions are estimated using photometric redshifts and do not extend beyond $z \sim 2$ (e.g. Caputi et al. 2007, hereafter C07). Second, the sources for which we are attempting to estimate the redshift distribution are the reddest ones whose SEDs are poorly fit by galaxy templates and for which photometric redshifts are the least reliable. Third, the optical luminosity distribution of $24\ \mu\text{m}$ sources is not known as a function of redshift. Although it is expected that fainter sources will lie at higher redshift (Figure 6), it is not clear how to implement this expectation and what the contribution to the counts might be, if any, from low-redshift dwarfs. Finally, we note that our spectroscopic redshift sample shows a clear trend of $R - [24]$ color with redshift, but the relation is broad and it is not clear if the sources that lack spectroscopic redshift measurements partake in the trend or are outliers. We made an attempt to implement a simple luminosity prior by extrapolating the evolving luminosity function as reported by C07. The results for all of the Keck+AGES targets as well as for the subset of these with spectroscopic redshifts are shown in Figure 9. Using the Le Floch et al. (2005)

luminosity function extrapolated beyond $z = 1$ produces similar results. Compared to the C07 luminosity function, it more closely reproduces our spectroscopic redshift distribution at $z < 1$, with the exception of the small dip at $z \sim 0.75$. As one might expect, a simple luminosity prior results in weighting the redshift probability distribution of a given source to lower redshift. This would be balanced by the optical brightness prior, which would push faint sources to higher redshift. Depending on the redshift evolution assumed, the strength of the bump at $z \approx 2$ can be reduced in strength. However, since there is no knowledge of the forms or weights of the priors discussed, we present the redshift distribution in Figure 9 as the measured distribution (white histogram) and our simple prediction for the sources without spectroscopic redshifts as estimated from the spectroscopic data with no priors. These should be interpreted as likely bracketing the true redshift distribution of the 24 μm sources.

The presence of a peak at $z \sim 2$ has been difficult to establish in previous studies of the 24 μm redshift distribution. It was not detected by Pérez-González et al. (2005) but it was detected with high significance by Caputi et al. (2006). Uncertainties in the photometric redshifts may be responsible for this difference. Neither Pérez-González et al. (2005) nor Caputi et al. (2006) have very many ($\lesssim 25$) spectroscopic redshifts above $z = 1.5$ (See Figures 13 and 14 in the former and Figures 1 and 5 in the latter). As a result, the scatter in the photometric redshifts at $z > 1.5$ has not been quantified. Without this information, an assessment of the reality of a peak at $z \sim 2$ based on photometric redshifts is difficult. (For comparison, our Keck spectroscopic survey includes spectroscopic redshifts for 46 galaxies at $z > 1.5$.) Both P05 and C05 focused on sources down to 83 μJy . Our study suggests that even sources brighter than 300 μJy display this peak, although this is based on assumptions regarding the nature of the sources without detected emission lines.

Neural net and template-fitting techniques have been used to calculate photometric redshifts (Brodwin et al. 2006) for NDWFS sources detected by IRAC, including the sources presented in this work. These photometric redshifts are highly accurate for IRAC-selected galaxies and AGN out to $z = 1.5$ and $z = 3$, respectively. An analysis of 24 μm selected galaxies with spectroscopic redshifts shows that their photometric redshifts are accurate out to $z \sim 1$, where the 24 μm sample is dominated by normal galaxies and LIRGs. At higher redshifts, corresponding to ULIRGs, the photometric redshifts become unreliable (the redshift dispersion in $\sigma/(1+z)$ is 0.13 with 95% clipping). Since it is likely that the Keck sources without spectroscopic redshifts lie at $z > 1$, we cannot use these photometric redshifts to determine their redshift distribution.

There are two reasonable interpretations of the $z \sim 2$ peak in the redshift distribution. The first is that there is a significant population of infrared-luminous sources with strong 7.7 and 8.6 μm PAH features. These sources have increasing detectability at $1.6 < z < 2$ and decreasing detectability at $2 < z < 3$ as the PAH emission shifts in and out of the 24 μm bandpass. The sources comprising the $z \sim 2$ peak have $f_\nu(24\mu\text{m}) \geq 300 \mu\text{Jy}$, and are therefore ULIRGs with infrared luminosities $L_{8-1000\mu\text{m}} > 3 \times 10^{12} L_\odot$ (assuming the tem-

plates of Chary & Elbaz (2001)). In the local universe, galaxies with these luminosities typically have low PAH equivalent widths (Lutz et al. 1998; Tran et al. 2001; Desai et al. 2007). However, there are sources at $z \sim 2$ that are known to be both extremely luminous and have strong PAH features (Lutz et al. 2005; Yan et al. 2005; Menéndez-Delmestre et al. 2007; Sajina et al. 2007), indicating that the relationship between PAH equivalent width and luminosity may be evolving in the sense that extremely luminous galaxies at high redshift have spectral properties similar to less luminous galaxies at low redshift (Sajina et al. 2007; Desai et al. 2007). Such an evolution might be expected if the PAH equivalent width is a function of various evolving sources properties (e.g. the distribution of star formation and the presence of an AGN). If the relationship between luminosity and spectral properties does evolve, then it is reasonable that a significant fraction of the sources composing the $z \sim 2$ peak have large PAH equivalent widths. This is an important effect to include in phenomenological models of galaxy evolution, such as those discussed in the next subsection.

A second explanation for the shape of the redshift distribution at $z > 1.6$ is that there is a large population of sources at these redshifts with deep 9.7 μm silicate absorption features. As discussed above, similar sources could be at least partly responsible for the decline in the redshift distribution between $z \sim 0.8$ and $z \sim 1.6$ because of decreasing detectability as the 24 μm bandpass samples the absorption feature. In contrast, these sources are more likely to be detected at $z \sim 2$, where the 24 μm bandpass is sampling rest-frame wavelengths shortward of the absorption feature. In this scenario, the $z \sim 2$ peak represents the reappearance of highly absorbed sources as the silicate absorption feature moves out of the 24 μm bandpass. The decrease at $z > 2$ would then be due to a combination of a decline in the flux density at wavelengths shorter than 8 μm and the fact that fewer galaxies meet the flux density cut at higher redshift in the absence of evolution.

We have qualitatively argued that the $z \sim 2$ bump could consist of some combination of sources with large PAH equivalent widths and sources with power-law continua accompanied by significant silicate absorption. Is there any evidence that either of these populations dominates? Figure 9 shows that a small fraction of the sources in the $z \sim 2$ peak have been spectroscopically confirmed. Of the 33 Keck targets with $1.6 < z < 3$, 73% show spectroscopic signatures of AGN activity (lines broader than 2000 km s^{-1} in the rest frame or the presence of high-ionization lines such as NV λ 1240, CIV λ 1549, HeII λ 1640, [NeV] λ 3346, or [NeV] λ 3426). The remaining 27% are of unknown type. Of the AGN, 50% are Type 1 AGN (with lines broader than 2000 km s^{-1}). Thus, a significant fraction of the spectroscopically confirmed sources in the $z \sim 2$ peak are AGN. However, these represent a small fraction of all of the galaxies in the peak, leaving the nature of the majority unknown.

IRAC colors have been used by several authors to identify sources that have power-law SEDs and therefore presumably contain powerful AGN (Stern et al. 2005; Lacy et al. 2004, 2007). Using the photometry from the IRAC Shallow Survey of the NDWFS Boötes field (Eisenhardt et al. 2004), Figure 10 shows the IRAC

color-color diagram for all of the Keck targets without spectroscopic redshifts. Sajina et al. (2005) have modelled the IRAC color-color diagram, and have delineated regions expected to be occupied by starbursts and AGN at various redshifts. Given the uncertainties involved, the redshift distribution implied by the IRAC colors is comparable to that deduced from the spectral coverage of the spectra. For example, the fraction of starforming galaxies at $z < 1.6$ suggested by the IRAC colors is similar to the total number of “no- z ” sources expected to lie at $z < 1.6$ according to Figure 8.

Given this concurrence, we assume that the vast majority of sources in the IRAC AGN wedge lie at $z > 1.6$. According to Figure 8, 75% of sources at $z > 1.6$ are expected to lie in the $z \sim 2$ peak, which we define to include all galaxies in the range $1.6 < z < 3$. If the fraction of AGN-dominated galaxies at $z > 1.6$ reflects the fraction within the $z \sim 2$ peak, then about $63\% \times 75\% = 47\%$ of sources without spectroscopic redshifts that lie within the $z \sim 2$ peak (50 out of 106 sources) are AGN-dominated.

We have already mentioned that 73% of the 33 spectroscopically confirmed sources within the $z \sim 2$ peak show optical spectroscopic signatures of AGN activity. Figure 10 shows that 85% of these fall within the IRAC AGN wedge. In fact, 82% (27 of 33) of all of the spectroscopically confirmed sources within the $z \sim 2$ peak lie within the AGN wedge. Only two AGES sources lie within the $z \sim 2$ peak (see Figure 9).

Based on the proportion of sources within the AGN wedge, we estimate that $(50 + 27) / (106 + 33) = 55\%$ of sources (including those with and without detected emission lines) within the $z \sim 2$ peak are AGN-dominated. As mentioned in Section 1, Caputi et al. (2006) have used photometric redshifts to estimate the redshift distribution of $24 \mu\text{m}$ sources down to $80 \mu\text{Jy}$. As in the current work, they also detect a peak at $z \sim 2$, which they interpret as the result of a population of starburst-dominated sources. This is not necessarily in contradiction with our results, since their flux limit is significantly fainter than ours. As shown in Brand et al. 2006 and Dey et al. 2008, the fraction of sources dominated by star formation is expected to increase with decreasing $24 \mu\text{m}$ flux density. Indeed, Figure 5 in Caputi et al. 2006 shows that most of the sources in their $z \sim 2$ peak fall below the $24 \mu\text{m}$ flux density limit of our survey.

The Infrared Spectrograph (IRS; Houck et al. 2004) on board the *Spitzer Space Telescope* has been used to obtain mid-infrared spectra of a sizeable number of optically faint ($R > 23$ mag), infrared bright ($f_{\nu}(24\mu\text{m}) > 750 \mu\text{Jy}$) sources (Houck et al. 2005; Yan et al. 2005; Weedman et al. 2006; Sajina et al. 2007; Dey et al. 2008). The IRS spectra of such sources tend to have power-law continua indicative of AGN activity, and some of these also exhibit silicate absorption features implying $z \sim 2$. Near-infrared spectra of a similar sample also reveal high redshifts and rest-frame optical spectroscopic signatures of AGN activity (Brand et al. 2007). At least some of the sources in the $z \sim 2$ peak have similar R -band magnitudes and $24 \mu\text{m}$ flux densities as these samples (see shaded histograms in Figure 6). However, many of the sources in the $z \sim 2$ peak are substantially fainter. There is some evidence that the contribution of star formation to the bolometric lumi-

osity of a galaxy increases with decreasing $24 \mu\text{m}$ flux density (Brand et al. 2006; Dey et al. 2008). If this is the case, then it is possible that the fainter sources in the $z \sim 2$ peak display strong PAH emission, which is typical in starburst galaxies. Near-infrared or mid-infrared IRS spectroscopy of the Keck targets without redshifts would help clarify the presence of the $z \sim 2$ peak and the energy generation mechanisms of the sources that comprise it.

6.2. Comparison with Models

In the previous subsection, we qualitatively discussed the possible origins of the observed features of the redshift distribution shown in Figure 9. We found that quantitative models are required for a robust interpretation of these features. In this subsection, we compare our observations to the predictions of several such models which have been found in the literature.

In Figure 11, we compare the observed redshift distribution to that predicted by four models of the evolution of mid-infrared sources. The models are described in detail by Chary & Elbaz (2001), Lagache et al. (2004), Gruppioni et al. (2005), and Pearson (2005); hereafter referred to as CE01, L04, G05, and P05, respectively. Below, we briefly describe the major elements of these models.

CE01 evolve the local mid-infrared luminosity function to fit the spectrum of the cosmic infrared background and the galaxy counts at mid-infrared, far-infrared, and sub-millimeter wavelengths. They constructed a family of luminosity-dependent template SEDs spanning the luminosities of normal galaxies, starbursts, LIRGs, and ULIRGs. In their model, all galaxies with $L_{8-1000\mu\text{m}} > 10^{10.2} L_{\odot}$ evolve, while only 5% of galaxies with lower luminosities evolve. The luminosity evolution goes as $(1+z)^{4.5}$ up to $z = 0.8$, after which it remains constant. The density evolution goes as $(1+z)^{1.5}$ out to $z = 0.8$, after which it goes as $(1+z)^{-0.4}$.

L04 follow the evolution of “normal” and starburst galaxies. Each of these galaxy types is represented by luminosity-dependent SEDs. The magnitude of the luminosity and density evolution in these populations was chosen to fit the existing observed mid- and far-infrared number counts, the mid- and far-infrared redshift distributions, the far-infrared luminosity functions, the far-infrared background, and its fluctuations. The resulting model features a very high rate of evolution of the luminosity density of starburst galaxies, peaking at $z \sim 0.7$ and remaining constant up to $z = 4$. The normal galaxies evolve out to $z = 0.4$, after which their luminosity density remains constant.

G05 start with the $15 \mu\text{m}$ luminosity function of galaxies and AGN. They assume that four populations contribute: “normal” galaxies, starburst galaxies, Type 1 AGN, and Type 2 AGN. They constrain the luminosity and density evolution of these populations by requiring a match to the observed $15 \mu\text{m}$ number counts. In this model, the normal population does not evolve. Meanwhile, the starburst population evolves strongly out to $z = 1$, as $(1+z)^{3.5}$ in luminosity and as $(1+z)^{3.8}$ in density. Type I AGN evolve in luminosity as $(1+z)^{2.6}$ out to $z = 2$, with no evolution at higher redshifts. Type II AGN evolve in luminosity as rapidly as $(1+z)^{2.6}$ out to $z = 2$ and do not evolve at higher redshifts.

P05 present two phenomenological models tracking the evolution of four classes of galaxies: normal, starburst, LIRG/ULIRG, and AGN. Both models are anchored to observed, type-dependent, local mid-infrared luminosity functions. In the “bright-end” model, the starbursts and AGN evolve in both luminosity and density as $(1+z)^{3.3}$ out to $z = 1$, and do not evolve at higher redshifts. The LIRG/ULIRG component evolves in luminosity as $(1+z)^{2.5}$ and in density as $(1+z)^{3.5}$ out to $z = 1$, and does not evolve at higher redshifts. In the “burst” model, the starburst population behaves as it did in the “bright-end” model. However, the LIRG/ULIRG component evolves in density as $(1+z)^7$ out to $z = 1$ and then more slowly in both density and luminosity to higher redshifts.

For a fair comparison with the observations, all of the models shown in Figure 11 have been computed down to $f_\nu(24\mu\text{m}) = 300 \mu\text{Jy}$ and have been normalized to the number of 24 μm sources targeted by our Keck observations (591). The observed redshift distributions shown in Figure 11 have been binned in redshift identically to the models for easy comparison. Because the models all have different binsizes, which are also different from the binsize used in Figure 9, the observations look slightly different in each panel and in Figure 9.

In comparing the models to the observations in Figure 11, we note that the detailed structure of the observed redshift distribution at $z > 1.5$ is not well-constrained, for the reasons described in §5.2. However, the relative number of sources at $z < 1$ and $z > 1$ should be a robust statistic with which to compare models and observations, since the vast majority of the Keck sources without spectroscopic redshifts are extremely unlikely to lie at $z < 1$. The observations indicate that 45% of the Keck+AGES targets lie at $z > 1$. In the CE01 and G05 models, only $\sim 25\%$ of the sources lie at $z > 1$. The templates used in these models may be insufficient to reproduce the observations. The CE01 model lacks both highly absorbed AGN-dominated sources and high-luminosity sources with strong PAH features, both of which could induce a peak at $z \sim 2$, as discussed in §6.1. The G05 model includes no dependence of PAH strength on luminosity. Although they include AGN-dominated sources, none have deep silicate absorption.

In contrast, the L04 and P05 models correctly predict the fraction of sources at $z > 1$. In both models, these high-redshift sources are starburst-dominated ULIRGs with strong PAH features. However, we suggested in §6.1 that absorbed power-law (AGN-dominated) SEDs likely also contribute to a trough at $z \sim 1.5$ which appears as a peak at $z \sim 2$. Although the relative numbers of $z < 1$ and $z > 1$ galaxies in the L04 and P05 models are consistent with our observations, further modelling is needed to determine whether an equally consistent model could be built with a higher fraction of AGN-dominated sources at $z > 1$. In addition, the exact position of the $z \sim 2$ peak is critical to testing the L04 and P05 models. This would require additional spectroscopy in the near- or mid-infrared.

7. CONCLUSIONS

We have conducted a redshift survey of 591 bright ($f_\nu(24\mu\text{m}) \geq 300 \mu\text{Jy}$) MIPS sources in the NDWFS Boötes field. We obtained emission line redshifts for 71%

of our targets, and have developed an algorithm to derive the redshift distribution of the remaining 29%. Using the entire distribution, we conclude:

1. The redshift distribution of bright 24 μm sources peaks at $z \sim 0.3$. There are no strong spectral features entering the 24 μm bandpass at the appropriate redshifts to cause this peak. It is therefore likely caused either by evolution in the luminosity function or by the fact that larger volumes are probed at higher redshifts, possibilities which can be tested with models.
2. There is a marginally-detected additional peak at $z \sim 0.9$. If real, it could be due to the fact that 24 μm surveys are more sensitive at this redshift to LIRGs with strong 12.7 μm PAH features and/or 12.8 μm [NeII] line emission. Additional data are needed to test the validity of this peak. The cleanest method would be to continue our spectroscopic survey of 24 μm sources to build up the sample size. Another approach would be to compute photometric redshifts for all of the 24 μm sources in the Boötes field, trading redshift accuracy (reasonable for photometric redshifts less than $z \sim 1$) for a larger sample size.
3. We find weak evidence for another peak at $z \sim 2$, consisting mainly of sources for which we were unable to determine emission-line redshifts, but whose redshift distribution we have estimated by assuming that the lack of emission lines is due to the limited wavelength coverage of the Keck spectrographs. Such a peak would be expected due to the increased sensitivity to starforming ULIRGs at redshifts where their 7.7 and 8.6 μm PAH features pass through the 24 μm bandpass. Alternatively, the peak could be the result of decreased sensitivity to heavily obscured AGN at redshifts where their 9.7 μm silicate absorption features pass through the 24 μm filter. Based on the arguments presented in the next paragraph, we suggest that the latter is an important effect.
4. We suggest that 55% of the sources in the $z \sim 2$ peak are AGN-dominated, and the remaining 45% are starburst-dominated. This suggestion is based mainly on the diversity of IRAC colors among the Keck targets without redshifts. In addition, AGN signatures are present in the optical spectra of 73% of the few (33) spectroscopically-confirmed sources within the $z \sim 2$ peak. Finally, sources similar to the brightest ($f_\nu(24\mu\text{m}) > 750 \mu\text{Jy}$) Keck targets without spectroscopic redshifts have AGN-like near- and mid-infrared spectra.
5. Of the four existing phenomenological models of galaxy formation that we considered, those that include a significant number of PAH-rich (and therefore presumably star-formation dominated) ULIRGs at $z > 1.5$ best reproduce the relative number of galaxies observed at $z < 1$ and $z > 1$. However, it remains to be shown that models including a significant fraction of AGN-dominated ULIRGs at $z > 1$ cannot also fit the observations.

We appreciate the referee's thoughtful feedback, which led to significant improvements in the paper. We thank Ranga-Ram Chary, David Elbaz, Carlotta Gruppioni, Guilaine Lagache, and Chris Pearson for providing the predictions of their models. We thank Chris Kochanek, Daniel Eisentein, and the AGES Team for providing access to the AGES database. AD thanks the Spitzer Science Center for their hospitality while this paper was being written. This work is based in part on observations made with the *Spitzer Space Telescope*, which is operated by the Jet Propulsion Laboratory, California Institute of Technology under a contract with NASA. Support for this work was provided by NASA through an award issued by JPL/Caltech. The *Spitzer* MIPS survey of the Boötes region was obtained using GTO time provided by the *Spitzer* Infrared Spectrograph Team (PI: James

Houck) and by M. Rieke. This work made use of images and data products provided by the NOAO Deep Wide-Field Survey (Jannuzi & Dey 1999), which is supported by the National Optical Astronomy Observatory (NOAO). NOAO is operated by AURA, Inc., under a cooperative agreement with the National Science Foundation. The authors wish to recognize and acknowledge the very significant cultural role and reverence that the summit of Mauna Kea has always had within the indigenous Hawaiian community. We are most fortunate to have the opportunity to conduct observations from this mountain.

Facilities: Keck:I (LRIS), Keck:II (DEIMOS), MMT (Hectospec), Mayall (MOSAIC-I), Spitzer (MIPS, IRAC, IRS)

REFERENCES

- Allen, D. A., Norris, R. P., Meadows, V. S., & Roche, P. F. 1991, *MNRAS*, 248, 528
- Altieri, B. et al. 1999, *A&A*, 343, L65
- Armus, L., Heckman, T. M., & Miley, G. K. 1989, *ApJ*, 347, 727
- Aussel, H., Cesarsky, C. J., Elbaz, D., & Starck, J. L. 1999, *A&A*, 342, 313
- Babbedge, T. S. R. et al. 2006, *MNRAS*, 370, 1159
- Blain, A. W., Smail, I., Ivison, R. J., Kneib, J.-P., & Frayer, D. T. 2002, *Physics Reports*, 369, 111
- Brand, K. et al. 2007, *ApJ*, 663, 204
- . 2006, *ApJ*, 644, 143
- Brodwin, M. et al. 2006, *ApJ*, 651, 791
- Caputi, K. I. et al. 2006, *ApJ*, 637, 727
- . 2007, *ApJ*, 660, 97
- Chapman, S. C., Blain, A. W., Smail, I., & Ivison, R. J. 2005, *ApJ*, 622, 772
- Chapman, S. C., Richards, E. A., Lewis, G. F., Wilson, G., & Barger, A. J. 2001, *ApJ*, 548, L147
- Chary, R. et al. 2004, *ApJS*, 154, 80
- Chary, R., & Elbaz, D. 2001, *ApJ*, 556, 562
- Connolly, A. J., Szalay, A. S., Dickinson, M., Subbarao, M. U., & Brunner, R. J. 1997, *ApJ*, 486, L11+
- Cowie, L. L., Barger, A. J., Fomalont, E. B., & Capak, P. 2004, *ApJ*, 603, L69
- Cowie, L. L., Songaila, A., Hu, E. M., & Cohen, J. G. 1996, *AJ*, 112, 839
- Cutri, R. M., Huchra, J. P., Low, F. J., Brown, R. L., & Vanden Bout, P. A. 1994, *ApJ*, 424, L65
- Desai, V. et al. 2007, *astro-ph/0707.4190*
- Dey, A. et al. 2008, *astro-ph/0801.1860*
- Dole, H. et al. 2004, *ApJS*, 154, 87
- Duc, P.-A., Mirabel, I. F., & Maza, J. 1997, *A&AS*, 124, 533
- Dwek, E. et al. 1998, *ApJ*, 508, 106
- Eisenhardt, P. R. et al. 2004, *ApJS*, 154, 48
- Elbaz, D. et al. 1999, *A&A*, 351, L37
- Faber, S. M. et al. 2003, in *Instrument Design and Performance for Optical/Infrared Ground-based Telescopes*. Edited by Iye, Masanori; Moorwood, Alan F. M. *Proceedings of the SPIE*, Volume 4841, pp. 1657-1669 (2003), 1657-1669
- Fabricant, D. et al. 2005, *PASP*, 117, 1411
- Fazio, G. G. et al. 2004, *ApJS*, 154, 10
- Finkbeiner, D. P., Davis, M., & Schlegel, D. J. 2000, *ApJ*, 544, 81
- Fixsen, D. J., Dwek, E., Mather, J. C., Bennett, C. L., & Shafer, R. A. 1998, *ApJ*, 508, 123
- Flores, H. et al. 1999, *ApJ*, 517, 148
- Gallego, J., Zamorano, J., Aragon-Salamanca, A., & Rego, M. 1995, *ApJ*, 455, L1+
- Gehrels, N. 1986, *ApJ*, 303, 336
- Giavalisco, M. et al. 2004, *ApJ*, 600, L103
- Gispert, R., Lagache, G., & Puget, J. L. 2000, *A&A*, 360, 1
- Gruppioni, C., Lari, C., Pozzi, F., Zamorani, G., Franceschini, A., Oliver, S., Rowan-Robinson, M., & Serjeant, S. 2002, *MNRAS*, 335, 831
- Gruppioni, C., Pozzi, F., Lari, C., Oliver, S., & Rodighiero, G. 2005, *ApJ*, 618, L9
- Hacking, P., Houck, J. R., & Condon, J. J. 1987, *ApJ*, 316, L15
- Hauser, M. G. et al. 1998, *ApJ*, 508, 25
- Heavens, A., Panter, B., Jimenez, R., & Dunlop, J. 2004, *Nature*, 428, 625
- Hogg, D. W., Cohen, J. G., Blandford, R., & Pahre, M. A. 1998, *ApJ*, 504, 622
- Houck, J. R. et al. 2004, *ApJS*, 154, 18
- . 2005, *ApJ*, 622, L105
- Jannuzi, B. T., & Dey, A. 1999, in *ASP Conf. Ser. 191: Photometric Redshifts and the Detection of High Redshift Galaxies*, 111+
- Juneau, S. et al. 2005, *ApJ*, 619, L135
- Kim, D.-C., Veilleux, S., & Sanders, D. B. 1998, *ApJ*, 508, 627
- Kleinmann, D. E., & Low, F. J. 1970a, *ApJ*, 161, L203+
- . 1970b, *ApJ*, 159, L165+
- Kleinmann, S. G., Hamilton, D., Keel, W. C., Wynn-Williams, C. G., Eales, S. A., Becklin, E. E., & Kuntz, K. D. 1988, *ApJ*, 328, 161
- Lacy, M., Petric, A. O., Sajina, A., Canalizo, G., Storrie-Lombardi, L. J., Armus, L., Fadda, D., & Marleau, F. R. 2007, *AJ*, 133, 186
- Lacy, M. et al. 2004, *ApJS*, 154, 166
- Lagache, G. et al. 2004, *ApJS*, 154, 112
- Lagache, G., & Puget, J. L. 2000, *A&A*, 355, 17
- Lagache, G., Puget, J.-L., & Dole, H. 2005, *ARA&A*, 43, 727
- Lagache, G., Puget, J.-L., & Gispert, R. 1999, *Ap&SS*, 269, 263
- Le Floc'h, E. et al. 2005, *ApJ*, 632, 169
- Lilly, S. J., Le Fevre, O., Hammer, F., & Crampton, D. 1996, *ApJ*, 460, L1+
- Low, J., & Kleinmann, D. E. 1968, *AJ*, 73, 868
- Lutz, D., Spoon, H. W. W., Rigopoulou, D., Moorwood, A. F. M., & Genzel, R. 1998, *ApJ*, 505, L103
- Lutz, D., Valiante, E., Sturm, E., Genzel, R., Tacconi, L. J., Lehnert, M. D., Sternberg, A., & Baker, A. J. 2005, *ApJ*, 625, L83
- Madau, P., Ferguson, H. C., Dickinson, M. E., Giavalisco, M., Steidel, C. C., & Fruchter, A. 1996, *MNRAS*, 283, 1388
- Marleau, F. R., Fadda, D., Appleton, P. N., Noriega-Crespo, A., Im, M., & Clancy, D. 2007, *ApJ*, 663, 218
- Marleau, F. R. et al. 2004, *ApJS*, 154, 66
- Massey, P., & Gronwall, C. 1990, *ApJ*, 358, 344
- Massey, P., Strobel, K., Barnes, J. V., & Anderson, E. 1988, *ApJ*, 328, 315
- Menéndez-Delmestre, K. et al. 2007, *ApJ*, 655, L65
- Metcalf, L. et al. 2003, *A&A*, 407, 791
- Oke, J. B. 1990, *AJ*, 99, 1621
- Oke, J. B. et al. 1995, *PASP*, 107, 375
- Oliver, S. J. et al. 1997, *MNRAS*, 289, 471
- Papovich, C. et al. 2006, *AJ*, 132, 231
- . 2004, *ApJS*, 154, 70
- . 2007, *ApJ*, 668, 45
- Pearson, C. 2005, *MNRAS*, 358, 1417
- Pérez-González, P. G. et al. 2005, *ApJ*, 630, 82
- Puget, J.-L., Abergel, A., Bernard, J.-P., Boulanger, F., Burton, W. B., Desert, F.-X., & Hartmann, D. 1996, *A&A*, 308, L5+
- Rieke, G. H., & Low, F. J. 1972, *ApJ*, 176, L95+
- Rieke, G. H. et al. 2004, *ApJS*, 154, 25
- Rowan-Robinson, M. et al. 2005, *AJ*, 129, 1183
- Sajina, A., Lacy, M., & Scott, D. 2005, *ApJ*, 621, 256

- Sajina, A., Yan, L., Armus, L., Choi, P., Fadda, D., Helou, G., & Spoon, H. 2007, *ApJ*, 664, 713
- Sanders, D. B., Soifer, B. T., Elias, J. H., Madore, B. F., Matthews, K., Neugebauer, G., & Scoville, N. Z. 1988a, *ApJ*, 325, 74
- Sanders, D. B., Soifer, B. T., Elias, J. H., Neugebauer, G., & Matthews, K. 1988b, *ApJ*, 328, L35
- Serjeant, S. et al. 2001, *MNRAS*, 322, 262
- Smail, I., Ivison, R. J., & Blain, A. W. 1997, *ApJ*, 490, L5+
- Soifer, B. T., & Neugebauer, G. 1991, *AJ*, 101, 354
- Somerville, R. S., Lee, K., Ferguson, H. C., Gardner, J. P., Moustakas, L. A., & Giavalisco, M. 2004, *ApJ*, 600, L171
- Steidel, C. C., Adelberger, K. L., Giavalisco, M., Dickinson, M., & Pettini, M. 1999, *ApJ*, 519, 1
- Stern, D. et al. 2005, *ApJ*, 631, 163
- Tinsley, B. M. 1968, *ApJ*, 151, 547
- Tody, D. 1993, in *Astronomical Society of the Pacific Conference Series*, Vol. 52, *Astronomical Data Analysis Software and Systems II*, ed. R. J. Hanisch, R. J. V. Brissenden, & J. Barnes, 173–+
- Tran, Q. D. et al. 2001, *ApJ*, 552, 527
- Treyer, M. A., Ellis, R. S., Milliard, B., Donas, J., & Bridges, T. J. 1998, *MNRAS*, 300, 303
- Veilleux, S., Kim, D.-C., Sanders, D. B., Mazzarella, J. M., & Soifer, B. T. 1995, *ApJS*, 98, 171
- Veilleux, S., Sanders, D. B., & Kim, D.-C. 1997, *ApJ*, 484, 92
- Weedman, D. W. et al. 2006, *ApJ*, 651, 101
- Werner, M. W. et al. 2004, *ApJS*, 154, 1
- Wilson, G., Cowie, L. L., Barger, A. J., & Burke, D. J. 2002, *AJ*, 124, 1258
- Yan, L. et al. 2005, *ApJ*, 628, 604

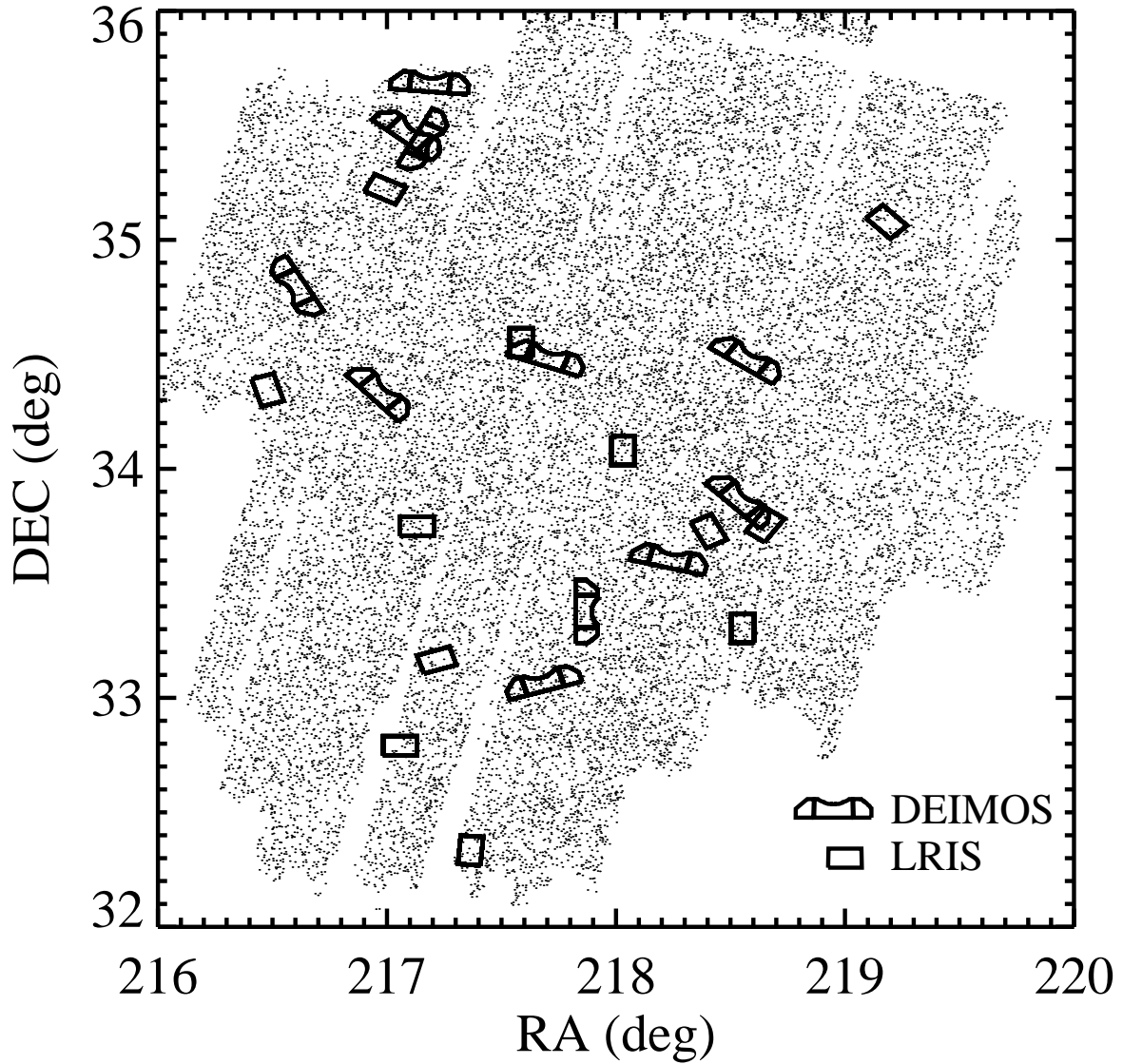


FIG. 1.— Schematic of Keck spectroscopic survey. Points indicate the locations of all Boötes sources with $f_{\nu}(24\mu\text{m}) \geq 300 \mu\text{Jy}$, the sample from which our optical spectroscopic targets were drawn. Overlaid are the positions of the LRIS and DEIMOS masks that comprise the spectroscopic survey. Mask positions were chosen to target rare sources with the most extreme infrared-to-optical flux density ratios. The final redshift distribution is corrected for this selection as described in §2. The total area of the spectroscopic survey is 0.33 deg^2 .

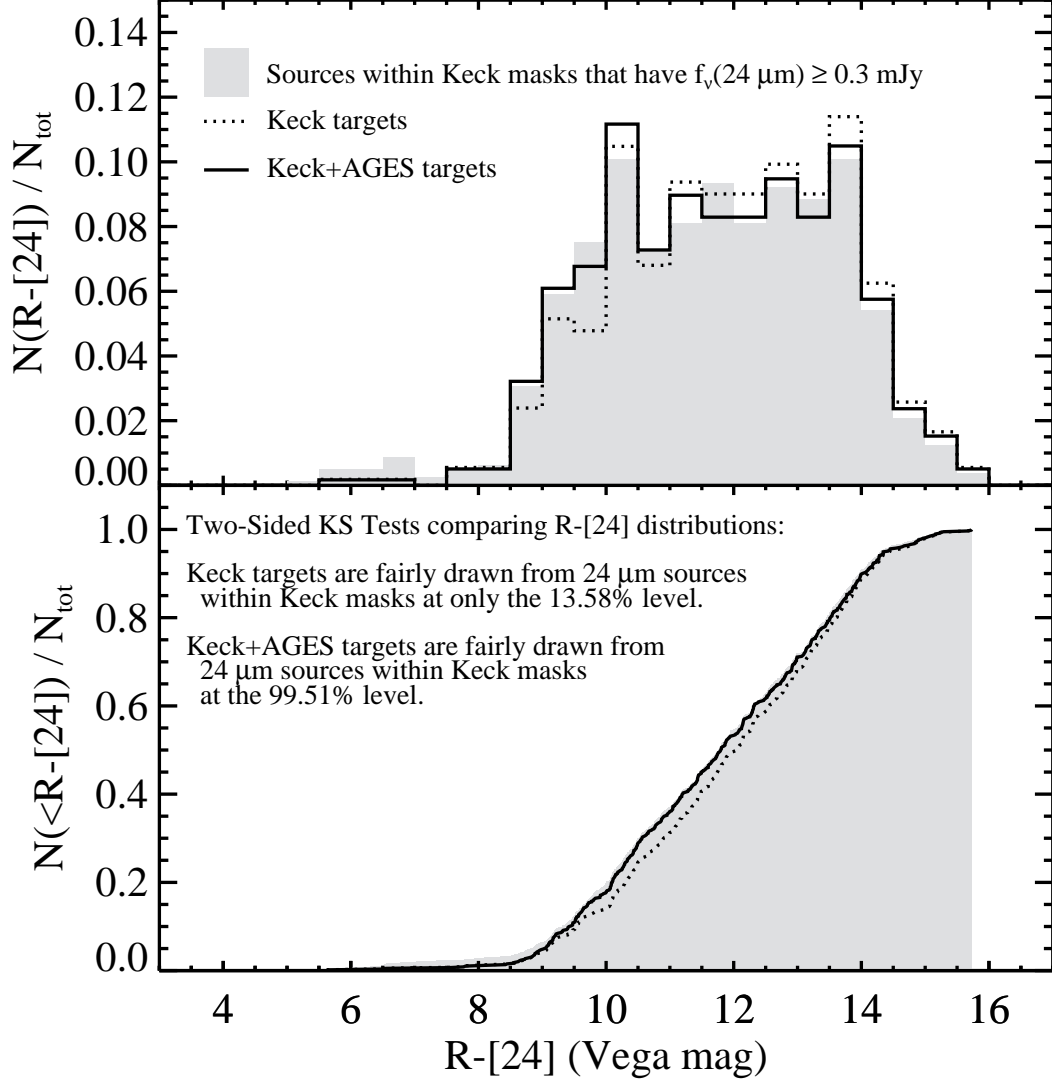


FIG. 2.— Differential (*top*) and cumulative (*bottom*) $R-[24]$ color distributions. Each of the distributions is normalized by the number of sources within the represented sample. Because of the targeting selection described in §2, the Keck targets include a disproportionately small fraction of sources with blue $R-[24]$ colors. Kolmogorov-Smirnov (KS) tests show that supplementing the Keck targets with additional redshifts from AGES results in a sample that is fairly drawn from the full 24 μm Boötes population in terms of $R-[24]$ color. KS tests also confirm that the 24 μm flux density and R -band magnitude distributions of the Keck+AGES sample are consistent with those of the full Boötes population.

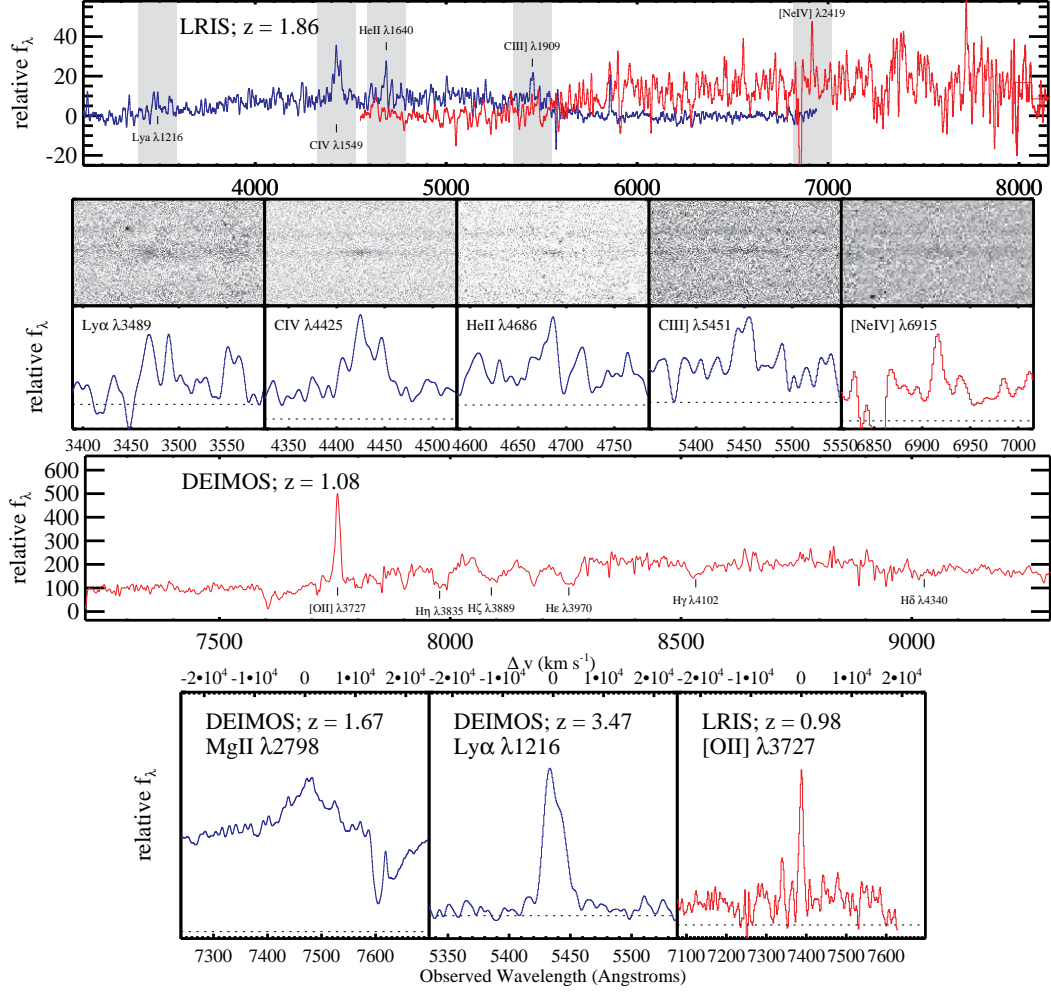


FIG. 3.— Example spectra. The top row shows an LRIS spectrum featuring multiple emission lines from which to determine a redshift. The grey shaded regions indicate regions around the lines that are shown in expanded form in the second (2D) and third (1D) rows. The fourth row shows a DEIMOS spectrum with only one emission line, but multiple absorption features allow for a robust redshift determination. In some spectra, only one emission line and no absorption lines were detected. In these cases, we identified the line by its shape, as illustrated in the fifth row. The zero-level fluxes are shown as dotted lines for each of the 1D snippets in the third and fifth rows.

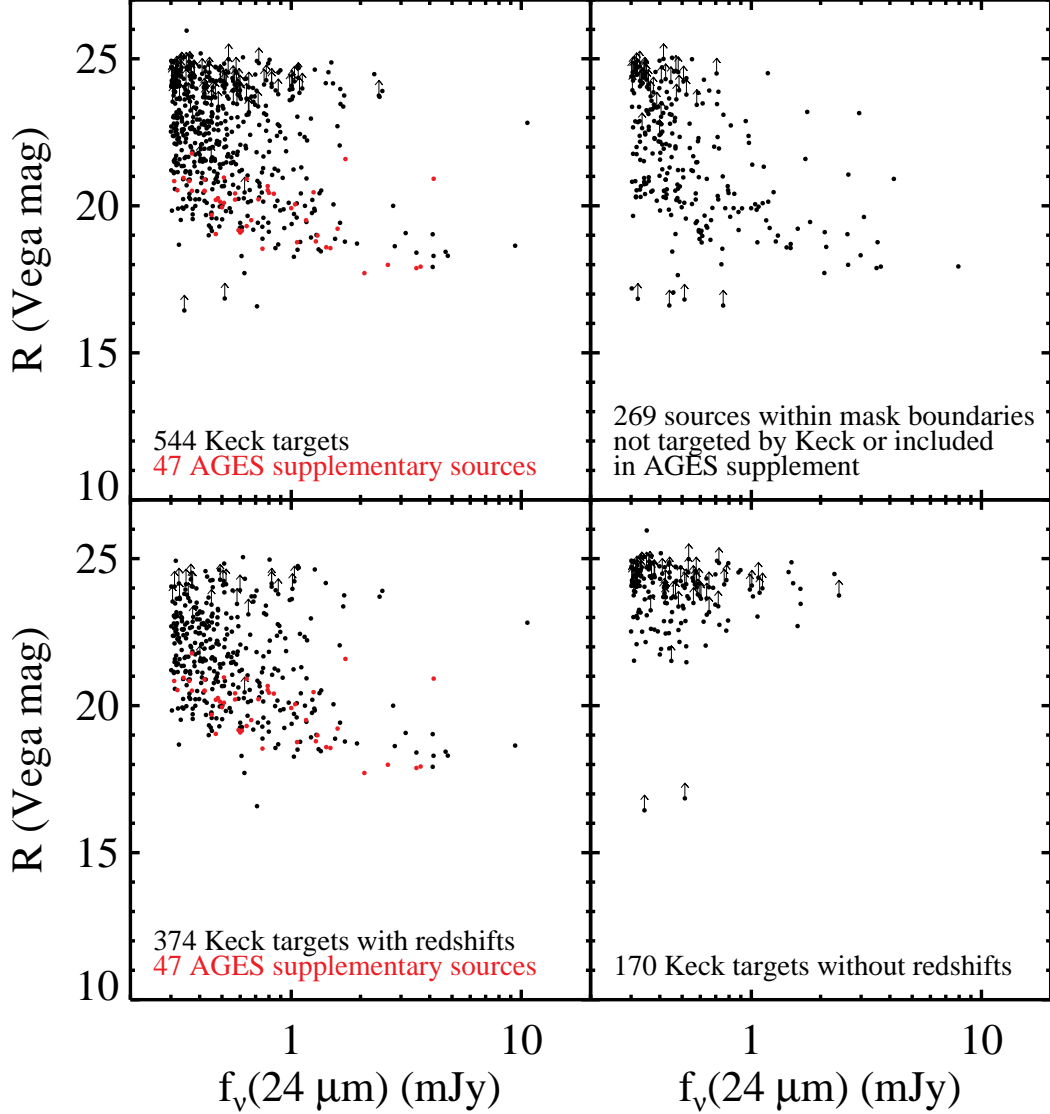


FIG. 4.— R -band magnitude versus MIPS $24\ \mu\text{m}$ flux density for various subsamples of the $24\ \mu\text{m}$ population within the Keck spectroscopic mask boundaries. This plot illustrates that (1) there is not a strong correlation between $24\ \mu\text{m}$ flux density and R -band magnitude; (2) the AGES supplement consists of sources with $R < 23$ mag that span a large range of $f_\nu(24\ \mu\text{m})$; (3) the distribution of Keck+AGES targets is similar to that of the untargted sources (visual confirmation that the Keck+AGES targets represent a fair subsample of $24\ \mu\text{m}$ sources); and (4) the Keck targets without spectroscopic redshifts tend to have faint R -band magnitudes but a range of $f_\nu(24\ \mu\text{m})$.

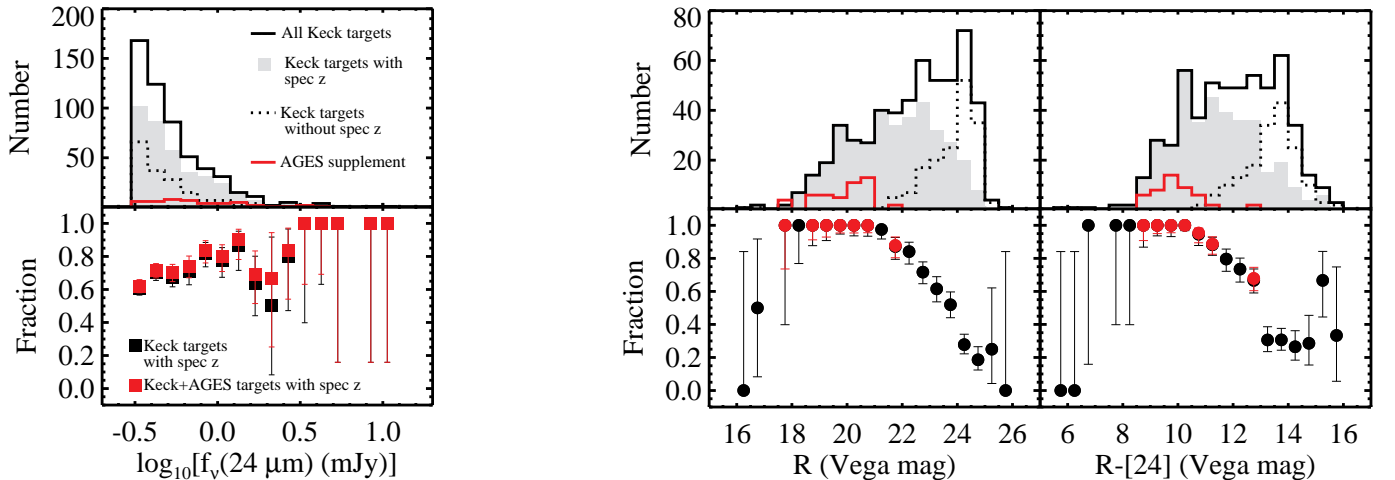


FIG. 5.— Number and fraction of sources as a function of $24\ \mu\text{m}$ flux density, R -band magnitude, and $R-[24]$ color. The error bars in the bottom panels include Poisson and binomial statistics (Gehrels 1986). The success rate of obtaining redshifts with Keck depends strongly on R -band magnitude, and much less on $f_\nu(24\ \mu\text{m})$.

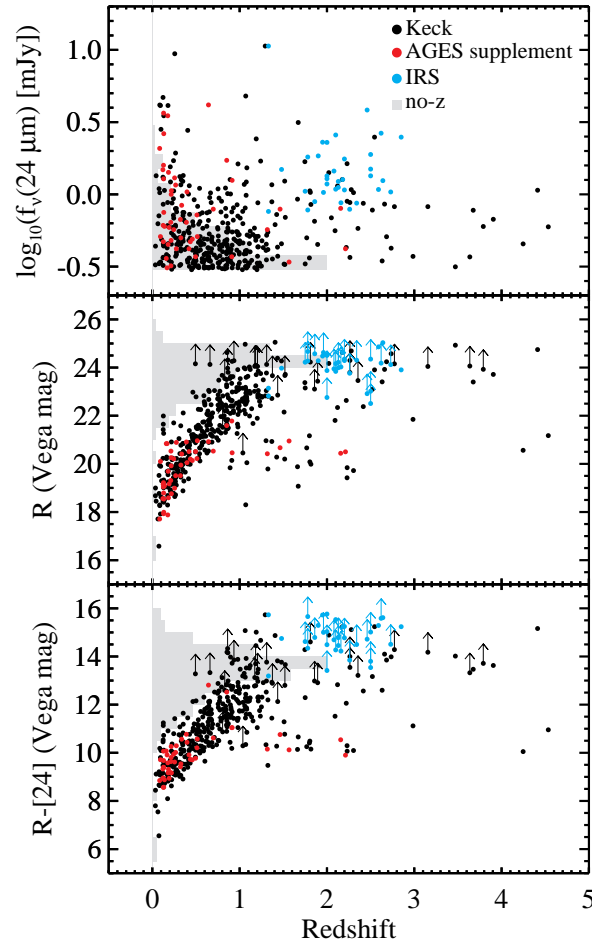


FIG. 6.— MIPS $24\ \mu\text{m}$ flux density, R -band magnitude, and $R - [24]$ color versus redshift. The points are color-coded by the source of the redshifts. The IRS redshifts are for a sample of Boötes sources (not necessarily within the Keck mask boundaries) taken from Houck et al. (2005). The $24\ \mu\text{m}$ flux density is not strongly correlated with redshift over any redshift range, while both the R -band magnitude and the $R - [24]$ color show a correlation for $z \lesssim 1$. However, the correlation is not tight enough and does not extend to high-enough redshifts to predict the redshifts of the Keck targets without spectroscopic redshifts, whose properties are indicated by the grey histograms.

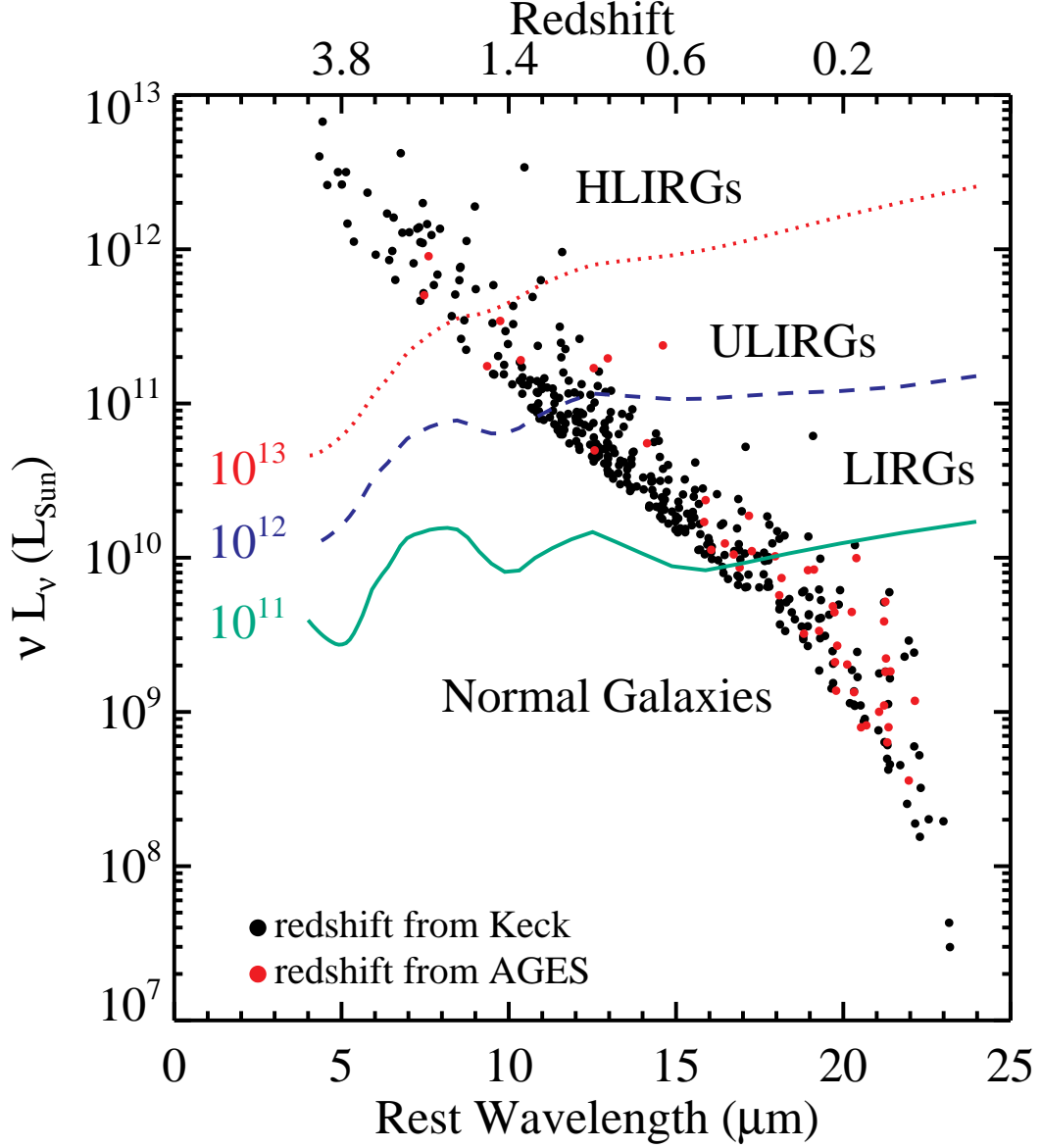


FIG. 7.— Luminosity (νL_ν) versus rest-frame wavelength for Keck+AGES targets with spectroscopic redshifts. Plotted quantities were computed using observed 24 μm flux densities and emission line redshifts. Also shown are the tracks for template sources with $L_{8-1000\mu\text{m}} = 10^{11} L_\odot$, $10^{12} L_\odot$, and $10^{13} L_\odot$ (Chary & Elbaz 2001). These models represent the boundaries between “normal” galaxies, luminous infrared galaxies (LIRGs), ultraluminous infrared galaxies (ULIRGs), and hyperluminous infrared galaxies (HLIRGs). For sources that match these templates the bolometric correction, i.e. $L_{8-1000\mu\text{m}}/\nu L_\nu(24/(1+z)\mu\text{m})$ is ~ 10 , ~ 10 and ~ 30 for LIRGs, ULIRGs and HLIRGs respectively.

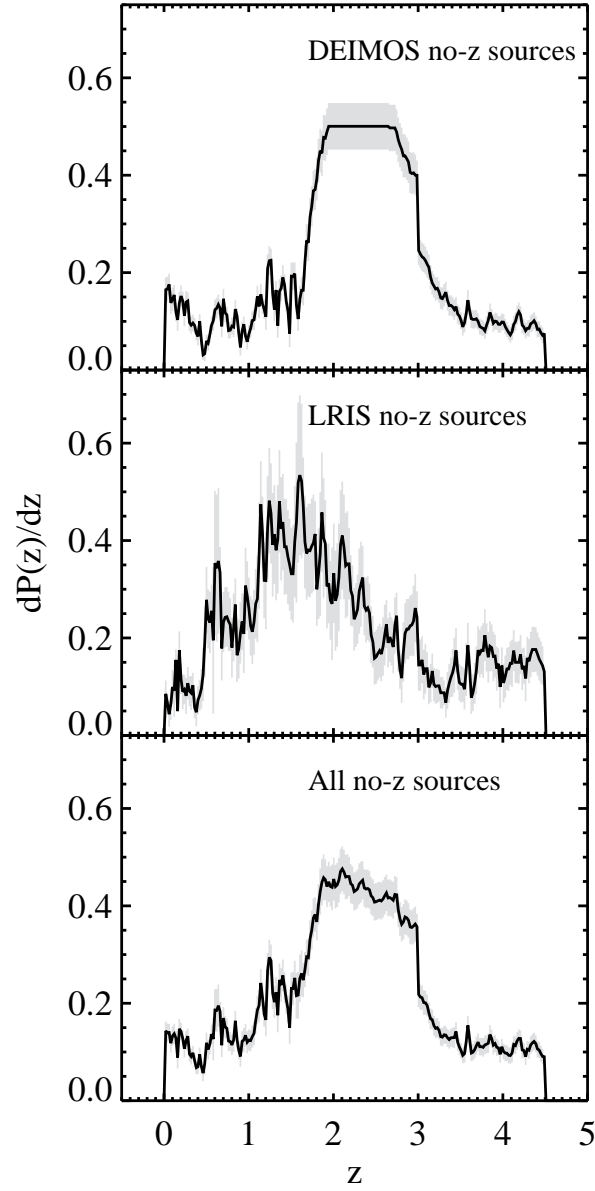


FIG. 8.— Estimated redshift probability density function (*black line*) and Poisson errors (*grey shaded region*) for Keck targets without spectroscopic redshifts. These functions were calculated by ruling out redshifts based on the non-detections of $\text{Ly}\alpha$, $[\text{OII}]\lambda 3727$, $\text{H}\beta$, and $\text{H}\alpha$, as described in §5.2. This method predicts that the redshift distribution of the “no- z ” sources peaks between $1.5 < z < 3$.

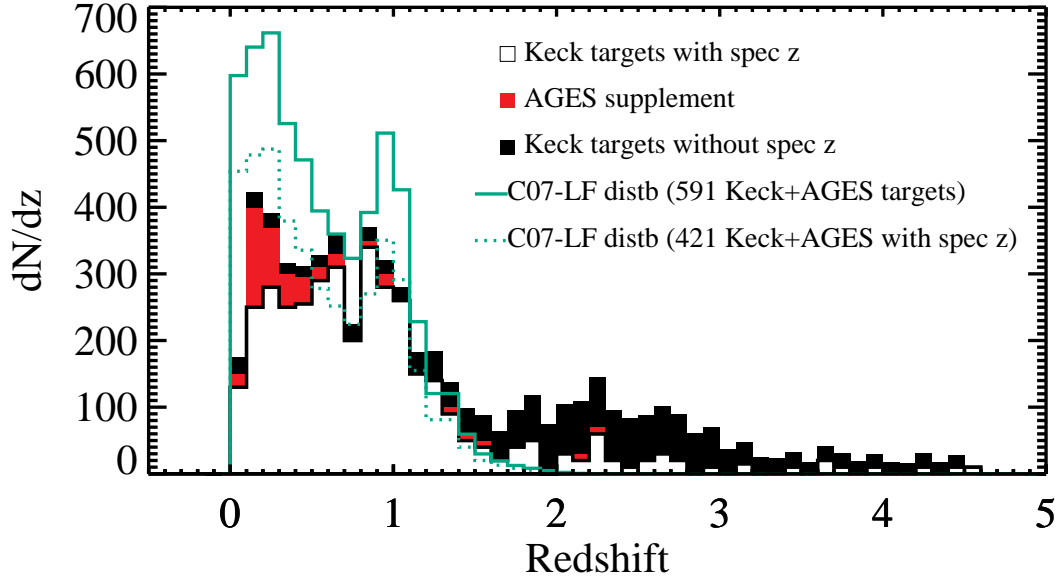


FIG. 9.— Observed redshift distribution of 24 μm sources down to $f_\nu(24) = 300 \mu\text{Jy}$. The redshift distribution peaks at $z \sim 0.3$, with a marginally-detected additional peak at $z \sim 0.9$. We find weak evidence for another peak at $z \sim 2$, based on estimates of the redshift distribution of the Keck targets without spectroscopic redshifts (see §5.2). The redshift distribution implied by the C07 $L_{8-1000\mu\text{m}}$ luminosity function is also shown, normalized to the number of sources in the entire Keck+AGES target list, and also to the subset with spectroscopic redshifts. The C07 luminosity function implies that the sources without spectroscopic redshifts lie at $z < 1$. We argue in §5.3 that this is unlikely.

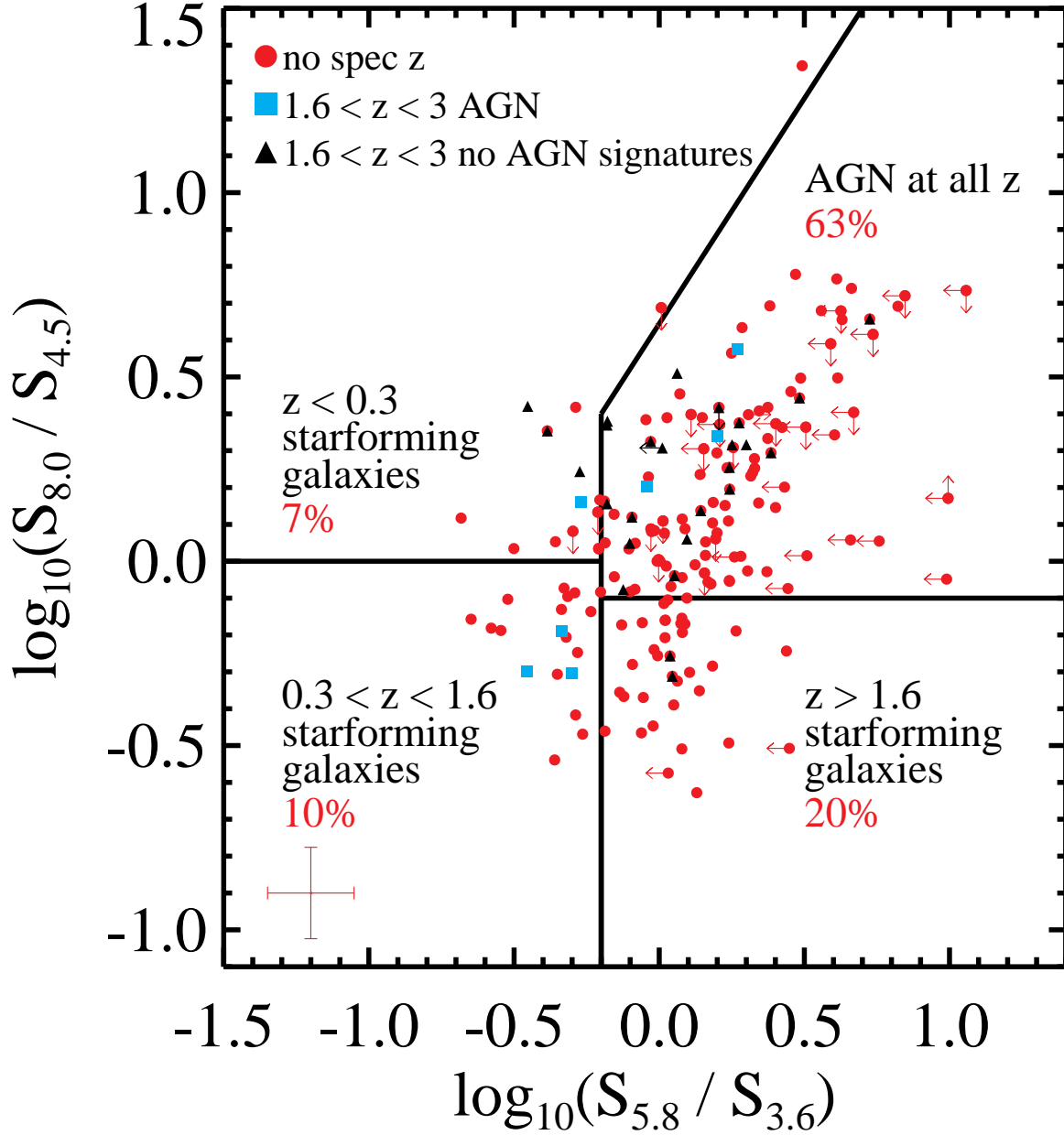


FIG. 10.— IRAC color-color diagram of Keck targets without spectroscopic redshifts and of Keck targets spectroscopically confirmed to lie within the $z \sim 2$ peak. The latter are color-coded by whether or not they show optical spectroscopic signatures of AGN activity. The error bars in the bottom left of the plot indicate the median errors for the plotted data. The black lines delineate the regions expected to be occupied by AGN and starbursts at various redshifts, according to the models of Sajina et al. (2005). The percentage labelled in each region indicate the percentage of red points that fall within them. We conclude that 55% of the sources within the $z \sim 2$ peak are AGN-dominated (see §6.1).

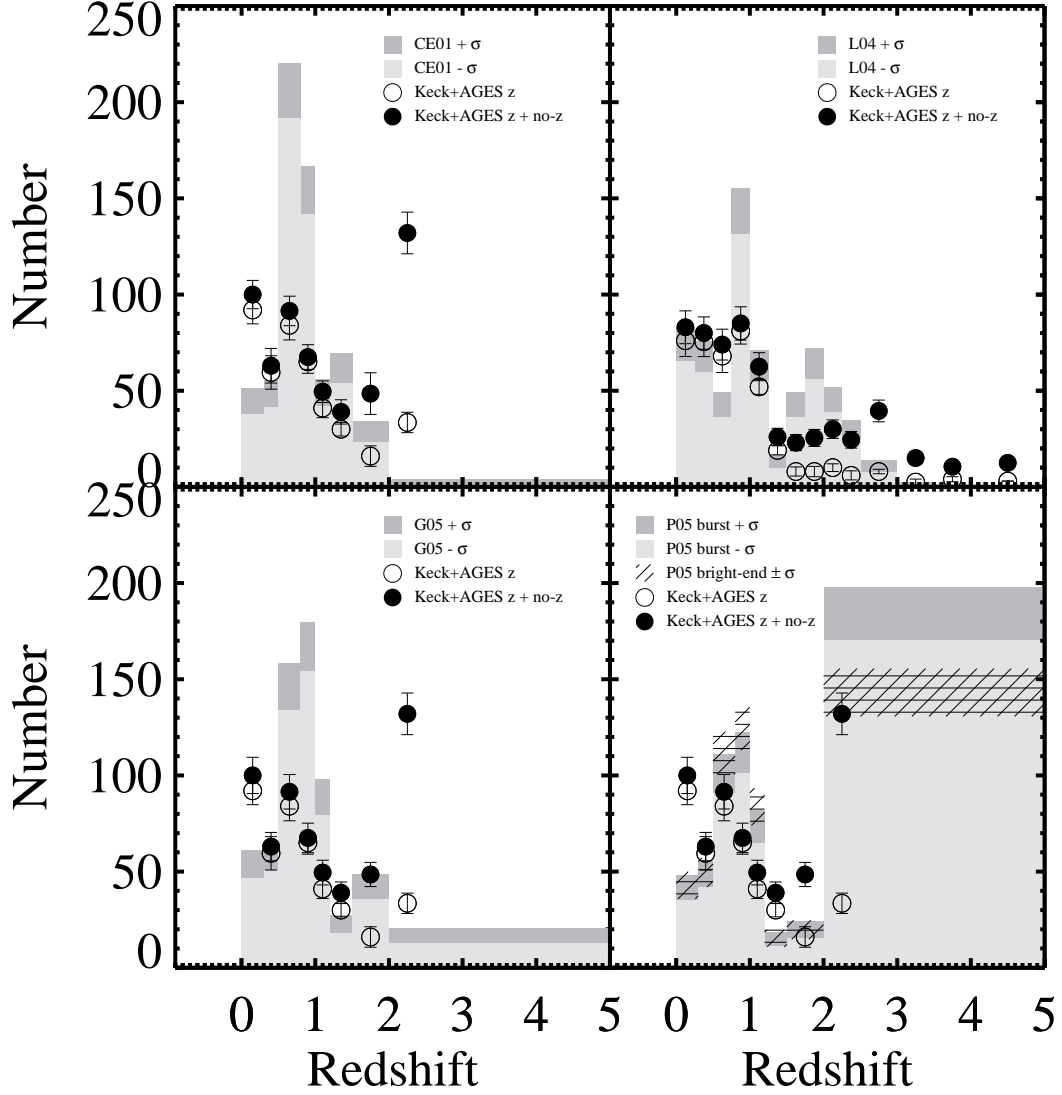


FIG. 11.— Observed redshift distribution of $24\ \mu\text{m}$ sources compared to the CE01, L04, G05, and P05 models. The models and their associated Poisson errors are shown as shaded histograms. P05 present two variants of their model: “burst” and “bright end”. All models have been normalized to the total number of Keck+AGES targets. The highest-redshift bin shows the number of counts at redshifts greater than its leftmost extent. The observed redshift distribution, binned identically to the models, is shown as points with 1σ Poisson error bars. None of the error bars include any contribution from cosmic variance. The L04 and P05 models, both of which predict a large fraction of PAH-rich ULIRGs at $z > 1.5$, best reproduce the observations.